Journal of the Mechanics and Physics of Solids 94 (2016) 316–335

Contents lists available at ScienceDirect

Journal of the Mechanics and Physics of Solids

journal homepage: www.elsevier.com/locate/jmps

Topology optimization of piezoelectric nanostructures

S.S. Nanthakumar [c], Tom Lahmer [c], Xiaoying Zhuang [d,g,*], Harold S. Park [e,*], Timon Rabczuk [a,b,c,f,**]

[a] Division of Computational Mechanics, Ton Duc Thang University, Ho Chi Minh City, Viet Nam
[b] Faculty of Civil Engineering, Ton Duc Thang University, Ho Chi Minh City, Viet Nam
[c] Institute of Structural Mechanics, Bauhaus-University Weimar, Marienstr. 15, D-99423 Weimar, Germany
[d] Department of Geotechnical Engineering, Tongji University, Shanghai, China
[e] Department of Mechanical Engineering, Boston University, 730 Commonwealth Avenue, ENA 212, Boston, MA 02215, United States
[f] School of Civil, Environmental and Architectural Engineering, Korea University, Seoul, Republic of Korea
[g] Institute of Continuum Mechanics, Leibniz University Hannover, AppelStr. 11, D-30167 Hannover

ARTICLE INFO

Article history:
Received 20 November 2015
Received in revised form
25 February 2016
Accepted 9 March 2016
Available online 12 May 2016

Keywords:
ZnO nanostructures
Surface piezoelectricity
Surface elasticity
Topology optimization

ABSTRACT

We present an extended finite element formulation for piezoelectric nanobeams and nanoplates that is coupled with topology optimization to study the energy harvesting potential of piezoelectric nanostructures. The finite element model for the nanoplates is based on the Kirchoff plate model, with a linear through the thickness distribution of electric potential. Based on the topology optimization, the largest enhancements in energy harvesting are found for closed circuit boundary conditions, though significant gains are also found for open circuit boundary conditions. Most interestingly, our results demonstrate the competition between surface elasticity, which reduces the energy conversion efficiency, and surface piezoelectricity, which enhances the energy conversion efficiency, in governing the energy harvesting potential of piezoelectric nanostructures.

© 2016 Elsevier Ltd. All rights reserved.

1. Introduction

Piezoelectric energy harvesters have garnered significant attention because of their ability to convert ambient mechanical energy into electrical energy (Priya, 2009, 2007). These energy harvesters have been utilized in a wide range of applications, where a review of vibration based energy harvesters is presented in Sodano et al. (2004).

Because of their wide usage, approaches to design piezoelectric energy harvesters with higher energy conversion efficiency have also been developed. One such approach is using computational topology optimization, where the geometry of the energy harvesters can be tuned to maximize the energy conversion efficiency. Examples of using topology optimization to design superior piezoelectric energy harvesters abound, including maximizing electromechanical conversion for a certain vibration mode (Silva and Kikuchi, 2007), designing a layout comprising the energy harvester as well as the electrical circuit (Rupp et al., 2009), and maximizing the energy conversion factor in cantilever plate energy harvesters subject to static loads (Zheng et al., 2009). There have also been works performing topology optimization of energy harvesters using different design variables, for example the densities that define the presence of piezoelectric material in each finite element

* Corresponding authors.
** Corresponding author at: Institute of Structural Mechanics, Bauhaus-University Weimar, Marienstr. 15, D-99423 Weimar, Germany.
E-mail addresses: xiaoying.zhuang@gmail.com (X. Zhuang), parkhs@bu.edu (H.S. Park), timon.rabczuk@tdt.edu.vn (T. Rabczuk).

http://dx.doi.org/10.1016/j.jmps.2016.03.027
0022-5096/© 2016 Elsevier Ltd. All rights reserved.

(Nakasone and Silva, 2009), or the geometry of elastic substructure (Wein et al., 2013). In Chen et al. (2010), an approach for designing the optimal configuration of a cantilever and a cylindrical piezoelectric energy harvesters with single and multiple materials was presented. A procedure for converting an inverse problem of detecting flaws in piezoelectric structures into an iterative optimization problem was given in Nanthakumar et al. (2013, 2014, 2016).

However, most piezoelectric energy harvesters have been developed using bulk materials. The exciting possibility of using nanoscale piezoelectric energy harvesters emerged in 2006 with the discovery of piezoelectricity from ZnO nanowires by Wang and Song (2006). Many researchers have since extended the original seminal work, including the development of self-powered nano generators that can provide gate voltage to effectively control charge transport (Wang and Song, 2006), lateral and vertical integration of ZnO nanowires into arrays that are capable of producing sufficient power to operate real devices (Xu et al., 2010), and the experimental determination that the piezoelectric coefficient d_{33} of ZnO nanobelt is much larger compared to bulk ZnO through measurements made using piezoresponse force microscope (Zhao et al., 2004). A recent review on the electromechanical properties and performance of ZnO, and other piezoelectric nanostructures, was performed by Espinosa et al. (2012).

Along with experimental work, there have been some recent theoretical studies into the piezoelectric properties of nanostructures and nanowires. Dai et al. (2011) highlighted the concept of surface piezoelectricity using a combination of theory and atomistic calculations, and then analyzed the (0001) surfaces of ZnO. Other works have also found that ZnO nanostructures exhibit different piezoelectric properties as compared to bulk ZnO (Mitrushchenkov et al., 2009; Momeni et al., 2012a), while surface effects on the piezoelectricity of ZnO nanowires were studied by Dai and Park (2013). Using quantum mechanical calculations, Agrawal and Espinosa (2011) found substantial increases in the piezoelectric properties of ZnO and GaN nanowires with decreasing size, while an increase of piezoelectric coefficient to 2.322 C/m^2 compared to a bulk value of 1.4 C/m^2 when the nanobelt thickness decreases to 0.8 nm was obtained using a molecular dynamics model by Momeni et al. (2012b).

Other researchers have developed analytic models for surface elasticity and surface piezoelectricity. For surface elasticity, the seminal work was that of Gurtin, Murdoch and co-workers (Gurtin and Murdoch, 1975; Gurtin et al., 1998), who were the first to establish a surface or interface elasticity model to capture surface stress and elastic effects. The elastic properties of nanostructures with surface and interface effects using the extended finite element method (XFEM) were proposed by Yvonnet et al. (2008), and later extended by Farsad et al. (2010) to study the mechanical behavior of homogeneous and composite nanobeams. For surface piezoelectricity, various analytic models have been developed, including an explicit formula for the electromechanical coupling coefficient considering surface effects (Yan and Jiang, 2011a) for piezoelectric nanowires, an Euler–Bernoulli beam theory for the vibrational and buckling behavior of piezoelectric nanobeams (Yan and Jiang, 2011b), and the electroelastic response of thin piezoelectric places considering surface effects using Kirchoff plate theory (Wang, 2012). It is also worth emphasizing that the electromechanical coupling, and nanoscale piezoelectricity, should also be impacted by surface elastic effects, as experiments have shown that ZnO nanowires with diameter smaller than about 100 nm exhibit a dramatic increase in elastic modulus as compared to bulk ZnO (Chen et al., 2006).

The objective of this work is to develop and apply topology optimization techniques to study how surface electromechanical effects impact the energy conversion efficiency of piezoelectric ZnO nanostructures. We accomplish this by discretizing the equations of surface piezoelectricity using the extended finite element method (XFEM), and using this numerical formulation to study energy harvesting from piezoelectric nanowires, nanoplates, and piezoelectric layers in energy harvesters accounting for both surface elastic and surface piezoelectric effects. Our results demonstrate the relative effects of both surface elasticity and piezoelectricity on the electromechanical energy conversion efficiency, while also elucidating the difference in performance of the nanoscale energy converters under both open and closed circuit boundary conditions.

2. Governing equations of surface piezoelectricity

We consider a piezoelectric domain Ω with a material surface Γ. Based on the continuum theory of surface piezoelectricity (Dai et al., 2011), the equilibrium equations are

$$\nabla\cdot\boldsymbol{\sigma} + \boldsymbol{b} = 0 \quad \text{in } \Omega \tag{1}$$

$$\nabla\cdot\mathbf{D} - \boldsymbol{q} = 0 \quad \text{in } \Omega \tag{2}$$

$$\nabla_{\boldsymbol{s}}\cdot\boldsymbol{\sigma}_S = 0 \quad \text{on } \Gamma \tag{3}$$

$$\nabla_{\boldsymbol{s}}\cdot\boldsymbol{D}_S = 0 \quad \text{on } \Gamma \tag{4}$$

where $\boldsymbol{\sigma}$ and $\mathbf{D}$ are mechanical stress and electric displacement, respectively, while $\boldsymbol{\sigma_s}$ and $\mathbf{D_s}$ are the surface stress and the surface electric displacement, respectively. In the above equation, $\nabla_{\boldsymbol{s}}\cdot\boldsymbol{\sigma_s} = \nabla\boldsymbol{\sigma}\colon \boldsymbol{P}$ and $\nabla_{\boldsymbol{s}}\cdot\boldsymbol{D_s} = \nabla\boldsymbol{D}\colon \boldsymbol{P}$ where : is the double tensor contraction and where $\boldsymbol{P}$ is a second order tensor defined as $\boldsymbol{P} = \boldsymbol{I} - \boldsymbol{n}\otimes\boldsymbol{n}$.

The linear piezoelectric constitutive relations for the bulk and surface are

$$\boldsymbol{\sigma} = \mathbb{C}\colon \boldsymbol{\epsilon} - \boldsymbol{e}\cdot\boldsymbol{E} \tag{5}$$

$$\boldsymbol{D} = \boldsymbol{e}\colon \boldsymbol{\epsilon} + \boldsymbol{\kappa}\cdot\boldsymbol{E} \tag{6}$$

$$\boldsymbol{\sigma_s} = \boldsymbol{\tau_s} + \mathbb{C}_s\colon \boldsymbol{\epsilon}_s - \boldsymbol{e_s}\cdot\boldsymbol{E_s} \tag{7}$$

$$\boldsymbol{D_s} = \boldsymbol{\omega_s} + \boldsymbol{e_s^T}\colon \boldsymbol{\epsilon_s} + \boldsymbol{\kappa}_s\cdot\boldsymbol{E}_s \tag{8}$$

where $\mathbb{C}$ and $\mathbb{C}_s$ are the fourth-order elastic stiffness tensors associated with the bulk and surface, respectively, while $\mathbf{e}$ and $\mathbf{e}_s$ correspond to the bulk and surface piezoelectric third order tensors, respectively. κ and κ_s are the bulk and surface second order permittivity tensors. $\boldsymbol{\tau_s}$ and $\boldsymbol{\omega_s}$ give the residual surface stresses and electric displacement, which are related to the residual surface strain and electric field, respectively. $\boldsymbol{\epsilon}$ and $\boldsymbol{E}$ are the bulk strain tensor and bulk electric field vector while $\boldsymbol{\epsilon_s}$ and $\boldsymbol{E_s}$ are their corresponding surface counterparts.

The surface energy density γ is given as

$$\gamma = \gamma_0 + \boldsymbol{\tau_s}\colon \boldsymbol{\epsilon_s} + \boldsymbol{\omega_s}\cdot\mathbf{E_s} + \frac{1}{2}\boldsymbol{\epsilon_s}\colon \mathbb{C}_s\colon \boldsymbol{\epsilon_s} + \frac{1}{2}\boldsymbol{E_s}\cdot\boldsymbol{\kappa_s}\cdot\boldsymbol{E_s} + \mathbf{E_s}\cdot\mathbf{e_s}\colon \boldsymbol{\epsilon_s} \tag{9}$$

where γ_0 is surface free energy density. Having defined the constitutive and field equations, we derive the weak form of the boundary value problem based on the principle of stationary potential energy. The total potential energy Π of the system is given by

$$\Pi = \Pi_{bulk} + \Pi_s - \Pi_{ext} \tag{10}$$

where Π_{bulk}, Π_s, and Π_{ext} represent the bulk internal energy, surface internal energy and the work of external forces, respectively, which are given by

$$\Pi_{bulk} = \frac{1}{2}\boldsymbol{\epsilon}\colon \mathbb{C}\colon \boldsymbol{\epsilon} - \boldsymbol{E}\cdot\mathbf{e}\colon \boldsymbol{\epsilon} - \frac{1}{2}\boldsymbol{E}\cdot\boldsymbol{\kappa}\cdot\boldsymbol{E} \tag{11}$$

$$\Pi_s = \int_\Gamma \gamma \, d\Gamma \tag{12}$$

The stationary condition of (10) is given by

$$D_{\delta\mathbf{u}}\Pi = 0 \tag{13}$$

where $D_{\delta\mathbf{u}}\Pi$ is the directional (or Gâteaux) derivative of the functional Π in the direction $\boldsymbol{\delta}\mathbf{u}$. Applying the stationary condition, the weak form of the equilibrium equations can be obtained by finding $\mathbf{u} \in \{\mathbf{u} = \bar{\mathbf{u}} \text{ on } \Gamma_u, \mathbf{u} \in H^1(\Omega)\}$ and $\boldsymbol{\phi} \in \{\boldsymbol{\phi} = \bar{\boldsymbol{\phi}} \text{ on } \Gamma_\phi, \boldsymbol{\phi} \in H^1(\Omega)\}$ such that

$$\begin{aligned}
&\int_\Omega \boldsymbol{\epsilon}(\delta\mathbf{u})\colon \mathbb{C}\colon \boldsymbol{\epsilon}(\mathbf{u})\, d\Omega - \int_\Omega \boldsymbol{E}(\delta\boldsymbol{\phi})\cdot\mathbf{e}\colon \boldsymbol{\epsilon}(\mathbf{u})\, d\Omega - \int_\Omega \boldsymbol{\epsilon}(\delta\mathbf{u})\colon \mathbf{e}\cdot\boldsymbol{E}(\boldsymbol{\phi})\, d\Omega - \int_\Omega \boldsymbol{E}(\delta\boldsymbol{\phi})\cdot\boldsymbol{\kappa}\cdot\boldsymbol{E}(\boldsymbol{\phi})\, d\Omega + \int_\Gamma \boldsymbol{\epsilon}_s(\delta\mathbf{u})\colon \mathbb{C}_s\colon \boldsymbol{\epsilon}_s(\mathbf{u})\, d\Gamma \\
&\quad - \int_\Gamma \boldsymbol{E}_s(\delta\boldsymbol{\phi})\cdot\mathbf{e}_s\colon \boldsymbol{\epsilon}_s(\mathbf{u})\, d\Gamma - \int_\Gamma \boldsymbol{\epsilon}_s(\delta\mathbf{u})\colon \mathbf{e}_s\cdot\boldsymbol{E}_s(\boldsymbol{\phi})\, d\Gamma - \int_\Gamma \boldsymbol{E}_s(\delta\boldsymbol{\phi})\cdot\boldsymbol{\kappa}_s\cdot\boldsymbol{E}_s(\boldsymbol{\phi})\, d\Gamma = -\int_\Gamma \boldsymbol{\epsilon}_s(\delta\mathbf{u})\colon \boldsymbol{\tau}_s\, d\Gamma \\
&\quad - \int_\Gamma \boldsymbol{E}_s(\delta\boldsymbol{\phi})\cdot\boldsymbol{\omega}_s\, d\Gamma + \int_{\Gamma_N} \delta\mathbf{u}\cdot\bar{\mathbf{t}}\, d\Gamma + \int_\Omega \delta\mathbf{u}\cdot\mathbf{b}\, d\Omega - \int_\Omega \delta\boldsymbol{\phi}\, q\, d\Omega
\end{aligned} \tag{14}$$

for all $\delta\mathbf{u} \in \{\delta\mathbf{u} = 0 \text{ on } \Gamma_u, \delta\mathbf{u} \in H^1(\Omega)\}$ and $\delta\boldsymbol{\phi} \in \{\delta\boldsymbol{\phi} = 0 \text{ on } \Gamma_\phi, \delta\boldsymbol{\phi} \in H^1(\Omega)\}$.

This weak formulation can be written in simplified form as

$$a(\mathbf{u}, \boldsymbol{\phi}, \delta\mathbf{u}, \delta\boldsymbol{\phi}) + a_s(\mathbf{u}, \boldsymbol{\phi}, \delta\mathbf{u}, \delta\boldsymbol{\phi}) = -l_s(\delta\mathbf{u}, \delta\boldsymbol{\phi}) + l(\delta\mathbf{u}, \delta\boldsymbol{\phi}) \tag{15}$$

3. XFEM formulation for surface piezoelectricity

The displacement field, $\boldsymbol{u^h}$ and electric potential field, $\boldsymbol{\phi^h}$ for a piezoelectric material in the XFEM formulation are expressed as:

$$\boldsymbol{u^h}(\mathbf{X}) = \sum_{i\in I} N_i(\mathbf{X})\boldsymbol{u_i} + \sum_{N=1}^{n_c}\sum_{l\in L} N_l(\mathbf{X})\boldsymbol{a_l^{(N)}} f_l^{(N)} \tag{16}$$

$$\boldsymbol{\phi^h}(\mathbf{X}) = \sum_{i\in I} N_i(\mathbf{X})\boldsymbol{\phi_i} + \sum_{N=1}^{n_c}\sum_{l\in L} N_l(\mathbf{X})\boldsymbol{\alpha_l^{(N)}} f_l^{(N)} \tag{17}$$

where $\boldsymbol{a_j}$ and $\boldsymbol{\alpha_j}$ are the additional degrees of freedom that account for the jump in displacement and electric potential field, respectively, n_c denotes the number of inclusion interfaces, L is the set of all nodes whose support is cut by the material

interface and $f^{(N)}$ in Eqs. (16) and (17) is the absolute signed distance function values from the interfaces. The interface enrichment is required because in the optimization process, the voids are assumed to be filled with a material that is 1000 times softer than the stiffness of the nano structure. This enables the optimization algorithm to recover from trial topologies in which the void boundary intersects with force boundary.

The terms in the weak formulation shown in the previous section can be written using the finite element (FE) approximation as follows:

$$a(\mathbf{u},\boldsymbol{\phi},\delta\mathbf{u},\delta\boldsymbol{\phi}) = \delta\mathbf{u}^T\Big(\int_\Omega \mathbf{B}_\mathbf{u}^\mathbf{T}\{\mathbb{C}\}\mathbf{B}_\mathbf{u}\,d\Omega\Big)\mathbf{u} + \delta\mathbf{u}^T\Big(\int_\Omega \mathbf{B}_\mathbf{u}^\mathbf{T}\{\mathbf{e}\}^T\mathbf{B}_\phi\,d\Omega\Big)\boldsymbol{\phi} + \delta\boldsymbol{\phi}^T\Big(\int_\Omega \mathbf{B}_\phi^\mathbf{T}\{\mathbf{e}\}\mathbf{B}_\mathbf{u}\,d\Omega\Big)\mathbf{u} - \delta\boldsymbol{\phi}^T\Big(\int_\Omega \mathbf{B}_\phi^\mathbf{T}\{\boldsymbol{\kappa}\}\mathbf{B}_\phi\,d\Omega\Big)\boldsymbol{\phi} \tag{18}$$

$$\begin{aligned} a_s(\mathbf{u},\boldsymbol{\phi},\delta\mathbf{u},\delta\boldsymbol{\phi}) &= \int_\Gamma (\mathbf{P}\boldsymbol{\varepsilon}(\delta\mathbf{u})\mathbf{P})^T\colon\{\mathbb{C}_s\}\colon(\mathbf{P}\boldsymbol{\varepsilon}(\mathbf{u})\mathbf{P})\,d\Gamma + \int_\Gamma (\mathbf{P}\boldsymbol{\varepsilon}(\delta\mathbf{u})\mathbf{P})^T\colon\{\mathbf{e}_s\}\cdot(\mathbf{P}_\phi\mathbf{E}(\boldsymbol{\phi}))\,d\Gamma \\ &\quad + \int_\Gamma (\mathbf{P}_\phi\mathbf{E}(\delta\boldsymbol{\phi}))^T\cdot\{\mathbf{e}_s\}\colon(\mathbf{P}\boldsymbol{\varepsilon}(\mathbf{u})\mathbf{P})\,d\Gamma - \int_\Gamma (\mathbf{P}_\phi\mathbf{E}(\delta\boldsymbol{\phi}))^T\cdot\{\boldsymbol{\kappa}_S\}\cdot(\mathbf{P}_\phi\mathbf{E}(\boldsymbol{\phi}))\,d\Gamma \\ &= \delta\mathbf{u}^T\Big(\int_\Gamma \mathbf{B}_\mathbf{u}^\mathbf{T}\mathbf{M}_\mathbf{p}^\mathbf{T}\{\mathbb{C}_s\}\mathbf{M}_\mathbf{p}\mathbf{B}_\mathbf{u}\,d\Gamma\Big)\mathbf{u} + \delta\mathbf{u}^T\Big(\int_\Gamma \mathbf{B}_\mathbf{u}^\mathbf{T}\mathbf{M}_\mathbf{p}^\mathbf{T}\{\mathbf{e}_s\}^T\mathbf{P}_\phi\mathbf{B}_\phi\,d\Gamma\Big)\boldsymbol{\phi} + \delta\boldsymbol{\phi}^T\Big(\int_\Gamma \mathbf{B}_\phi^\mathbf{T}\mathbf{P}_\phi^\mathbf{T}\{\mathbf{e}_s\}\mathbf{M}_\mathbf{P}\mathbf{B}_\mathbf{u}\,d\Gamma\Big)\mathbf{u} \\ &\quad - \delta\boldsymbol{\phi}^T\Big(\int_\Gamma \mathbf{B}_\phi^\mathbf{T}\mathbf{P}_\phi^\mathbf{T}\{\boldsymbol{\kappa}_s\}\mathbf{P}_\phi\mathbf{B}_\phi\,d\Gamma\Big)\boldsymbol{\phi} \end{aligned} \tag{19}$$

where $\mathbb{C}$ and $\mathbb{C}_s$ are the matrix forms of the fourth order elastic bulk and surface stiffness tensors, $\boldsymbol{e}$ and $\boldsymbol{e_s}$ are the matrix forms of the third order elastic bulk and surface coupling tensors, $\boldsymbol{\kappa}$ and $\boldsymbol{\kappa_s}$ are the matrix forms of the second order elastic bulk and surface stiffness tensors and $\boldsymbol{\varepsilon}$ and $\boldsymbol{\varepsilon}_s$ are the vector forms of the bulk and surface strain tensors.

The matrix $\boldsymbol{Mp}$ (Yvonnet et al., 2008) gives the relationship between surface strain $\boldsymbol{\epsilon_s}$ and the bulk strain $\boldsymbol{\epsilon}$ so that $\boldsymbol{\epsilon_s} = \boldsymbol{Mp}\,\boldsymbol{\epsilon}$ and takes the form:

$$\mathbf{M_P} = \begin{pmatrix} P_{11}^2 & P_{12}^2 & P_{11}P_{12} \\ P_{12}^2 & P_{22}^2 & P_{12}P_{22} \\ 2P_{11}P_{12} & 2P_{12}P_{22} & P_{12}^2 + P_{11}P_{22} \end{pmatrix} \tag{20}$$

$$l_s(\delta\mathbf{u},\delta\boldsymbol{\phi}) = \int_\Gamma (\mathbf{P}\boldsymbol{\varepsilon}(\delta\mathbf{u})\mathbf{P})^T\colon\boldsymbol{\tau_s}\,d\Gamma + \int_\Gamma (\mathbf{P}_\phi\mathbf{E}(\delta\boldsymbol{\phi}))^T\cdot\boldsymbol{\omega_s}\,d\Gamma = \delta\mathbf{u}^T\int_\Gamma \mathbf{B}_\mathbf{u}^\mathbf{T}\mathbf{M}_\mathbf{p}^\mathbf{T}\boldsymbol{\tau_s}\,d\Gamma + \delta\boldsymbol{\phi}^T\int_\Gamma \mathbf{B}_\phi^\mathbf{T}\mathbf{P}_\phi^\mathbf{T}\boldsymbol{\omega_s}\,d\Gamma \tag{21}$$

$$l(\delta\mathbf{u},\delta\boldsymbol{\phi}) = \delta\mathbf{u}^\mathbf{T}\Big(\int_{\Gamma_N}\mathbf{N}^T\bar{\mathbf{t}}\,d\Gamma + \int_\Omega \mathbf{N}^\mathbf{T}\mathbf{b}\,d\Omega\Big) - \delta\boldsymbol{\phi}^\mathbf{T}\int_\Omega \mathbf{N}^\mathbf{T}\mathbf{q}\,d\Omega \tag{22}$$

where $\boldsymbol{B_u}$ and $\boldsymbol{B_\phi}$ are the strain-displacement and electric field-potential matrices, respectively. In this work, we utilize the extended finite element method (XFEM) (Moes et al., 1999; Sukumar et al., 2001), to discretize the finite element equations given previously in Eqs. (18)–(22) and the weak form (14). We utilize XFEM, rather than the standard FEM in the present work due to its ability to represent evolving interfaces and discontinuities, which is essential in the topology optimization process.

From Eqs. (18)–(22) and the weak form (14), the system of algebraic XFEM equations to solve is

$$(\mathbf{K}_{\mathbf{uu}}^\mathbf{b} + \mathbf{K}_{\mathbf{uu}}^\mathbf{s})\boldsymbol{u} + (\mathbf{K}_{\boldsymbol{\phi u}}^\mathbf{b} + \mathbf{K}_{\boldsymbol{\phi u}}^\mathbf{s})\boldsymbol{\phi} = -(\boldsymbol{f}_\mathbf{u}^\mathbf{s} + \boldsymbol{f}_\mathbf{u}^{\mathbf{ext}}) \tag{23}$$

$$(\mathbf{K}_{\mathbf{u}\boldsymbol{\phi}}^\mathbf{b} + \mathbf{K}_{\mathbf{u}\boldsymbol{\phi}}^\mathbf{s})\boldsymbol{u} + (\mathbf{K}_{\boldsymbol{\phi\phi}}^\mathbf{b} + \mathbf{K}_{\boldsymbol{\phi\phi}}^\mathbf{s})\boldsymbol{\phi} = -(\boldsymbol{g}_\mathbf{u}^\mathbf{s} + \boldsymbol{g}_\mathbf{u}^{\mathbf{ext}}) \tag{24}$$

The vectors $\boldsymbol{u}$ and $\boldsymbol{\phi}$ comprise the corresponding FE and enriched DOFs. The $\boldsymbol{B_u}$ and $\boldsymbol{B_\phi}$ matrices and the specific form of the bulk and surface stiffness matrices can be found in Appendix B. The piezoelectric energy harvesters we consider are thin flexible structures, and so a Kirchoff plate theory adopted in Junior et al. (2009) is employed in this work. Details are given in Appendix C.

4. Topology optimization of nanoscale piezoelectric energy harvesters

4.1. Objective function

A common objective function in topology optimization of piezoelectric energy harvesters is to maximize the energy conversion. The electromechanical coupling coefficient (EMCC) k is defined as (Trinidade and Benjeddou, 2009)

$$k^2 = \frac{\Pi_m^2}{\Pi_e\, \Pi_d} \tag{25}$$

where Π_m is the elasto-dielectric energy and Π_e and Π_d are the stored elastic and dielectric energy respectively

$$\Pi_m = \int_\Omega \boldsymbol{\varepsilon}(\boldsymbol{u})^T \boldsymbol{e}^T \boldsymbol{E}(\boldsymbol{\phi})\, d\Omega \tag{26}$$

$$\Pi_e = \int_\Omega \boldsymbol{\varepsilon}(\boldsymbol{u})^T \boldsymbol{C} \boldsymbol{\varepsilon}(\boldsymbol{u})\, d\Omega \tag{27}$$

$$\Pi_d = \int_\Omega \boldsymbol{E}(\boldsymbol{\phi})^T \boldsymbol{\kappa} \boldsymbol{E}(\boldsymbol{\phi})\, d\Omega \tag{28}$$

The energy harvesting device is assumed to be subjected only to static mechanical loads and so the EMCC may be rewritten as (Chen et al., 2010)

$$k^2 = \frac{\Pi_d}{\Pi_e} \tag{29}$$

Clearly, the higher the EMCC the better from a piezoelectric energy harvesting point of view, which thus leads to the best performance of the energy harvesting device.

Within the XFEM numerical formulation, the shape and topology of the piezoelectric nanostructure is modified to maximize the energy conversion. This is done by defining the geometry of the nanostructure using the level set function. Doing so makes the design variable in the optimization problem the level set function Ψ. The corresponding objective function is:

$$\text{Minimize} \quad J(\Psi) = \frac{1}{k^2} = \frac{\Pi_e}{\Pi_d} \tag{30}$$

$$\text{Subject to} \quad \int_\Omega d\Omega - \bar{V} = 0 \tag{31}$$

$$a(\mathbf{u}, \boldsymbol{\phi}, \delta\mathbf{u}, \delta\boldsymbol{\phi}) + a_s(\mathbf{u}, \boldsymbol{\phi}, \delta\mathbf{u}, \delta\boldsymbol{\phi}) = -l_s(\delta\mathbf{u}, \delta\boldsymbol{\phi}) + l(\delta\mathbf{u}, \delta\boldsymbol{\phi}) \tag{32}$$

The optimum configuration is obtained by using the level set based topology optimization method described in the following section.

4.2. Level set method and sensitivity analysis

The level set method (LSM), which is a numerical technique to track moving interfaces and shapes, was originally proposed by Osher and Sethian (1988). The LSM has been used in structural sensitivity analysis, i.e. by Allaire et al. (2004) and Wang et al. (2007). In topology optimization, the LSM is valuable as it enables initially defined voids to merge, move and change shapes leading to a modified topology of the structure that minimizes the objective function. In the LSM, the optimal structures obtained are free from grayscale, since the structural boundaries are represented as the iso-surfaces of the level set function. The level set function is dynamically updated at each time step by solving the Hamilton–Jacobi (H–J) partial differential equation to minimize the objective function

$$\frac{\partial \psi}{\partial t} + V_n |\nabla \psi| = 0 \tag{33}$$

The above H–J equation is solved to obtain the updated level set function and thereby the updated topology of the design structure. In the present work, the level set function is parametrized using compactly supported radial basis functions. The CS-RBF designed by Wendland (1995) with C2 continuity shown in Eq. (34) is adopted

$$f(r) = \max\{0, (1-r)\}^4 (4r+1) \tag{34}$$

in which r is the support radius and is defined in 2D Euclidean space as

$$r(\boldsymbol{x}) = \frac{\sqrt{(x-x_i)^2 + (y-y_i)^2}}{d_{sp}} \tag{35}$$

The parameter d_{sp} determines the support size of a knot (x_i, y_i). The d_{sp} should be set appropriately to ensure that there are sufficient knots located in the neighborhood of any point of interest (x,y). In this work, the d_{sp} is chosen to be in the range of 2–4 times the average nodal spacing. The knots and FE nodes are considered to be coincident.

The resulting CS-RBF based interpolant for the implicit level set function (Wang and Wang, 2006) is expressed as

$$\psi(\boldsymbol{x}, t) = \boldsymbol{f}(\boldsymbol{x})^T \boldsymbol{\alpha}(t) = \sum_{i=1}^{n} f_i(\boldsymbol{x})\, \alpha_i \tag{36}$$

where $\boldsymbol{f}(\boldsymbol{x})$ is the CS-RBF defined in Eq. (34) that can be uniquely determined by the positions of the "n" scattered knots and $\boldsymbol{\alpha}$ is the vector of weights or expansion coefficients of the knots. Here it is assumed that the spatial and time dependency of level set function can be separated. Substituting Eq. (36) into Hamilton–Jacobi equation (33), reduces the HJ equation into an ODE as shown below:

$$\boldsymbol{f}^T \frac{d\boldsymbol{\alpha}}{dt} + V_n |(\nabla \boldsymbol{f})^T \boldsymbol{\alpha}| = 0 \tag{37}$$

The vector of expansion coefficients is updated as shown in the following equation leading to an improved topology in each iteration:

$$\boldsymbol{\alpha}(t^{n+1}) = \boldsymbol{\alpha}(t^n) + \Delta t \boldsymbol{A}^{-1} \boldsymbol{B}(\boldsymbol{\alpha}(t^n)) \tag{38}$$

where Δt is the time step, $\boldsymbol{A}$ is the collocation matrix,

$$\mathbf{A} = \begin{bmatrix} f_1(\boldsymbol{x_1}) & \cdots & f_n(\boldsymbol{x_1}) \\ \vdots & \ddots & \vdots \\ f_1(\boldsymbol{x_n}) & \cdots & f_n(\boldsymbol{x_n}) \end{bmatrix}$$
$$\mathbf{B}(\boldsymbol{\alpha}) = \begin{bmatrix} V_n(\boldsymbol{x_1}) |((\nabla f^T(\boldsymbol{x_1}))\boldsymbol{\alpha}| \\ \vdots \\ V_n(\boldsymbol{x_n}) |((\nabla f^T(\boldsymbol{x_n}))\boldsymbol{\alpha}| \end{bmatrix} \tag{39}$$

The velocity to update the level set function, V_n, is obtained by performing sensitivity analysis as discussed subsequently.

The material derivative approach and the related lemmas presented in Choi and Kim (2005) are adopted to determine the material time derivative of the objective function (see Appendix A for details):

$$\dot{J} = \frac{\dot{\Pi}_e(\boldsymbol{u}, \boldsymbol{u})}{\Pi_d(\boldsymbol{\phi}, \boldsymbol{\phi})} - \frac{\Pi_e(\boldsymbol{u}, \boldsymbol{u})\dot{\Pi}_d(\boldsymbol{\phi}, \boldsymbol{\phi})}{\Pi_d(\boldsymbol{\phi}, \boldsymbol{\phi})^2} \tag{40}$$

$$\dot{J} = C_1\, \dot{\Pi}_e(\boldsymbol{u}, \boldsymbol{u}) + C_2\, \dot{\Pi}_d(\boldsymbol{\phi}, \boldsymbol{\phi}) \tag{41}$$

$$\begin{aligned} \dot{\Pi}_e(\boldsymbol{u}, \boldsymbol{u}) = & \int_\Omega 2\, \boldsymbol{\varepsilon}(\boldsymbol{u}')^T \colon \mathbb{C}^{bulk} \colon \boldsymbol{\varepsilon}(\boldsymbol{u})\, d\Omega + \int_\Gamma \boldsymbol{\varepsilon}(\boldsymbol{u})^T \colon \mathbb{C}^{bulk} \colon \boldsymbol{\varepsilon}(\boldsymbol{u}) V_n\, d\Gamma \\ & + \int_\Gamma 2\boldsymbol{\varepsilon_s}(\boldsymbol{u}')^T \colon \mathbb{C}^s \colon \boldsymbol{\varepsilon_s}(\boldsymbol{u})\, d\Gamma + \int_\Gamma [\nabla(\boldsymbol{\varepsilon_s}(\boldsymbol{u})^T \colon \mathbb{C}^s \colon \boldsymbol{\varepsilon_s}(\boldsymbol{u})) \cdot n + (\boldsymbol{\varepsilon_s}(\boldsymbol{u})^T \colon \mathbb{C}^s \colon \boldsymbol{\varepsilon_s}(\mathbf{u}))\eta)]\, V_n\, d\Gamma \end{aligned} \tag{42}$$

$$\begin{aligned} \dot{\Pi}_d(\boldsymbol{\phi}, \boldsymbol{\phi}) = & \int_\Omega 2\, \boldsymbol{E}(\boldsymbol{\phi}')^T \cdot \boldsymbol{\kappa}^{bulk} \cdot \boldsymbol{E}(\boldsymbol{\phi})\, d\Omega + \int_\Gamma \boldsymbol{E}(\boldsymbol{\phi})^T \cdot \boldsymbol{\kappa}^{bulk} \cdot \boldsymbol{E}(\boldsymbol{\phi}) V_n\, d\Gamma + \int_\Gamma 2\, \boldsymbol{E_s}(\boldsymbol{\phi}')^T \cdot \boldsymbol{\kappa}^s \cdot \boldsymbol{E_s}(\boldsymbol{\phi})\, d\Gamma \\ & + \int_\Gamma [\nabla(\boldsymbol{E}(\boldsymbol{\phi})^T \colon \boldsymbol{\kappa}^s \cdot \boldsymbol{E_s}(\boldsymbol{\phi})) \cdot n + (\boldsymbol{E_s}(\boldsymbol{u})^T \cdot \boldsymbol{\kappa}^s \cdot \boldsymbol{E_s}(\boldsymbol{\phi}))\eta)]\, V_n\, d\Gamma \end{aligned} \tag{43}$$

$$C_1 = \frac{1}{\Pi_d(\boldsymbol{\phi}, \boldsymbol{\phi})} \tag{44}$$

$$C_2 = -\frac{\Pi_e(\boldsymbol{u}, \boldsymbol{u})}{\Pi_d(\boldsymbol{\phi}, \boldsymbol{\phi})^2} \tag{45}$$

The augmented Lagrangian L defining the unconstrained optimization problem is

$$L = J(\mathbf{u}, \boldsymbol{\phi}, \boldsymbol{\Omega}) + \chi(\boldsymbol{\Omega}) \tag{46}$$

The shape derivative of augmented Lagrangian L is defined as

$$L' = J'(\mathbf{u}, \boldsymbol{\phi}, \boldsymbol{\Omega}) + \chi'(\boldsymbol{\Omega}) \tag{47}$$

$$J' = \int_\Gamma \boldsymbol{G} \cdot \boldsymbol{V_n}\, d\Gamma \tag{48}$$

where

Table 1
Electromechanical properties of bulk ZnO.

Elastic constants	Piezoelectric constants	Dielectric constants
$C_{11}=206$ GPa $C_{12}=117$ GPa $C_{13}=118$ GPa $C_{33}=211$ GPa $C_{44}=44.3$ GPa	$e_{31}=-0.58$ C/m^2 $e_{33}=1.55$ C/m^2 $e_{15}=-0.48$ C/m^2	$\kappa_{11}=8.11$ C/(GV m) $\kappa_{33}=11.2$ C/(GV m)

$$\begin{aligned}\boldsymbol{G} = & \int_{\Omega} C_1\, \boldsymbol{\varepsilon}(\boldsymbol{u}')^T : \mathbb{C}^{bulk} : \boldsymbol{\varepsilon}(\boldsymbol{u})\, d\Omega + \int_{\Gamma} C_1\, \boldsymbol{\varepsilon_s}(\boldsymbol{u})^T : \mathbb{C}^s : \boldsymbol{\varepsilon_s}(\boldsymbol{u})\, d\Gamma \\ & + \int_{\Omega} C_2\, \boldsymbol{E}(\boldsymbol{\phi}')^T \cdot \boldsymbol{\kappa}^{bulk} \cdot \boldsymbol{E}(\boldsymbol{\phi})\, d\Omega + \int_{\Gamma} C_2\, \boldsymbol{E_s}(\boldsymbol{\phi})^T \cdot \boldsymbol{\kappa}^s \cdot \boldsymbol{E_s}(\boldsymbol{\phi})\, d\Gamma - \int_{\Gamma} \boldsymbol{\varepsilon_s}(\boldsymbol{w}) \boldsymbol{\tau_s} \cdot \eta\, d\Gamma - \int_{\Gamma} \boldsymbol{\varepsilon_s}(\boldsymbol{u})^T : \mathbb{C}^s : \boldsymbol{\varepsilon_s}(\boldsymbol{w}) \cdot \eta\, d\Gamma \\ & + \int_{\Gamma} \boldsymbol{\varepsilon_s}(\boldsymbol{u})^T : \mathbf{e}^{sT} \cdot \boldsymbol{E_s}(\boldsymbol{\psi}) \cdot \eta\, d\Gamma + \int_{\Gamma} \boldsymbol{E_s}(\boldsymbol{\phi})^T \cdot \boldsymbol{e}^s : \boldsymbol{\varepsilon_s}(\boldsymbol{w}) \eta\, d\Gamma \\ & + \int_{\Gamma} \boldsymbol{E_s}(\boldsymbol{\phi})^T \cdot \boldsymbol{\kappa}^s \cdot \boldsymbol{E_s}(\boldsymbol{\psi}) \eta\, d\Gamma - \int_{\Omega} \boldsymbol{\varepsilon}(\boldsymbol{u})^T : \mathbb{C}^{bulk} : \boldsymbol{\varepsilon}(\boldsymbol{w})\, d\Omega + \int_{\Omega} \boldsymbol{\varepsilon}(\boldsymbol{u})^T : \mathbf{e}^{bulkT} \cdot \boldsymbol{E}(\boldsymbol{\psi})\, d\Gamma + \int_{\Omega} \boldsymbol{E}(\boldsymbol{\phi})^T \cdot \boldsymbol{e}^{bulk} : \boldsymbol{\varepsilon}(\boldsymbol{w})\, d\Gamma \\ & + \int_{\Omega} \boldsymbol{E}(\boldsymbol{\phi})^T \cdot \boldsymbol{\kappa}^{bulk} \cdot \boldsymbol{E}(\boldsymbol{\psi})\, d\Omega \end{aligned} \tag{49}$$

Based on the steepest descent direction

$$\begin{aligned} \boldsymbol{G} &= -\boldsymbol{V_n} \\ J' &= -\int_{\Gamma} \boldsymbol{V_n^2}\, d\Gamma \le 0 \end{aligned} \tag{50}$$

In Eq. (49), $\boldsymbol{u}$ and $\boldsymbol{\phi}$ are the actual displacement and potential variables respectively, while $\boldsymbol{w}$ and $\boldsymbol{\psi}$ are the adjoint displacement and potential variables. The displacement $\boldsymbol{u}$ and voltage $\boldsymbol{\phi}$ are obtained by solving Eqs. (23) and (24). The weak formulation for the adjoint equation is derived in Appendix A. The system of algebraic equations of the adjoint problem is as follows:

$$(\boldsymbol{K_{uu}^b} + \boldsymbol{K_{uu}^s})\boldsymbol{w} + (\boldsymbol{K_{\phi u}^b} + \boldsymbol{K_{\phi u}^s})\boldsymbol{\psi} = 2C_1(\boldsymbol{K_{uu}^b} + \boldsymbol{K_{uu}^s})\boldsymbol{u} \tag{51}$$

$$(\boldsymbol{K_{u\phi}^b} + \boldsymbol{K_{u\phi}^s})\boldsymbol{w} + (\boldsymbol{K_{\phi\phi}^b} + \boldsymbol{K_{\phi\phi}^s})\boldsymbol{\psi} = 2C_2(\boldsymbol{K_{\phi\phi}^b} + \boldsymbol{K_{\phi\phi}^s})\boldsymbol{\phi} \tag{52}$$

5. Numerical examples

In this section we study the energy harvesting capability of a piezoelectric nanobeam, nanoplate and a cantilever energy harvester with nanoscale piezoelectric layers. We also perform topology optimization of these piezoelectric structures. We consider examples both with and without surface elasticity and piezoelectricity to examine the effects that surface effects have on the energy harvesting ability. In all examples, ZnO is the piezoelectric material of choice, where the surface elastic and piezoelectric properties of ZnO are shown in Tables 1 and 2 (Hoang et al., 2013).

5.1. Two-dimensional piezoelectric nanobeam

5.1.1. Finite element model validation

In our first example, we consider a two-dimensional cantilever beam of dimension 200 × 10 nm subject to constant mechanical load at the free end. The beam is meshed with 200 × 10 4-node bilinear quadrilateral (Q4) finite elements, and the poling direction is vertically upwards along the thickness direction. The bulk electromechanical coupling coefficient (EMCC$_b$) for this case can be analytically obtained by the following expression (Trinidade and Benjeddou, 2009):

Table 2
Electromechanical properties of ZnO surfaces.

Elastic constants	Piezoelectric constants
$C_{11}^s=44.2$ N/m $C_{12}^s=14.2$ N/m $C_{13}^s=14.2$ N/m $C_{33}^s=35$ N/m $C_{44}^s=11.7$ N/m	$e_{31}^s=-0.216$ nC/m $e_{33}^s=0.451$ nC/m $e_{15}^s=-0.253$ nC/m

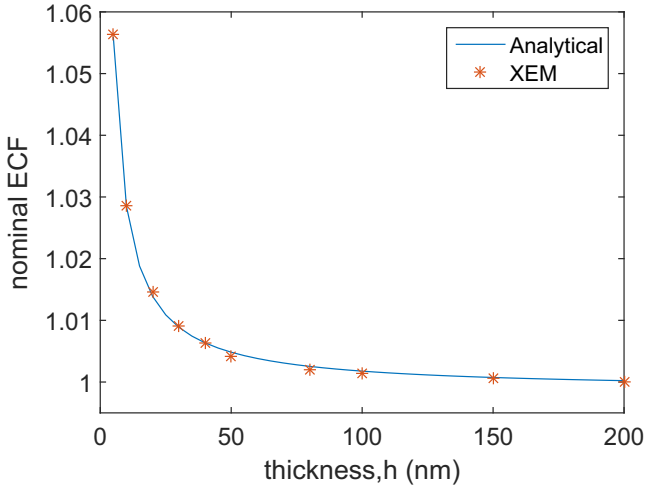

Fig. 1. Variation of nominal energy conversion factor with nanobeam thickness, with the beam aspect ratio constant at 20.

$$EMCC_b = \frac{e_{31}^2}{(C_{11}\kappa_{33} + e_{31}^2)} \tag{53}$$

The expression including surface effects can be obtained based on the derivation given in Yan and Jiang (2011a) for this example problem as

$$EMCC_s = \frac{h\, e_{31}^2 + 2\, e_{31} e_{31}^s}{h(C_{11}\kappa_{33} + e_{31}^2) + 2(C_{11}^s\kappa_{33} + e_{31} e_{31}^s)} \tag{54}$$

Fig. 1 shows the variation of ECF with increasing nanobeam depth for a constant aspect ratio of 20, where the y-axis of the figure plots the nominal EMCC, or the value $EMCC_s/EMCC_b$. This aspect ratio is chosen as it is clear in plane strain conditions from Eq. (54) that the ECF is dependent only on the nanobeam thickness. As expected the surface elastic and piezoelectric effects lose their significance as the thickness increases. The plot shows good agreement between XFEM and the analytical results, validating the proposed computational formulation.

5.1.2. Optimization of two-dimensional piezoelectric nanobeam

We now perform topology optimization of the two-dimensional nanobeams under both open and closed circuit boundary conditions to examine not only the enhancements in energy conversion that are possible, but also to delineate the relative effects of surface piezoelectricity and elasticity on the energy conversion. To do so, we again subject the cantilever nanobeam to a mechanical point load acting vertically downwards at its free end, while the nanobeam is poled along the thickness direction.

The nanobeam is placed over a substrate made of material with Young's modulus of $E = 150$ GPa, where the substrate dimensions are the same as the nanobeam, though surface effects on the substrate are neglected. As shown in Fig. 2, electrodes are placed above and below the nanobeam. Open circuit conditions are achieved by grounding the bottom electrode while the top electrode is free to take any potential value, while in closed circuit both the top and bottom electrodes are grounded.

To give an example of an illustrative optimal topology, we show in Fig. 3 the optimized nanobeam topology for a 40 $\times$

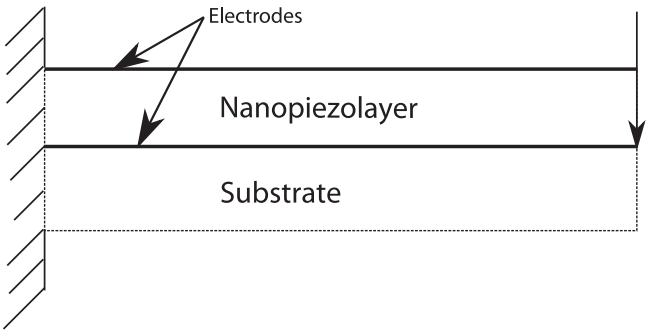

Fig. 2. A cantilever beam energy harvester with nano piezoelectric layer and a substrate subject to a point load at the free end.

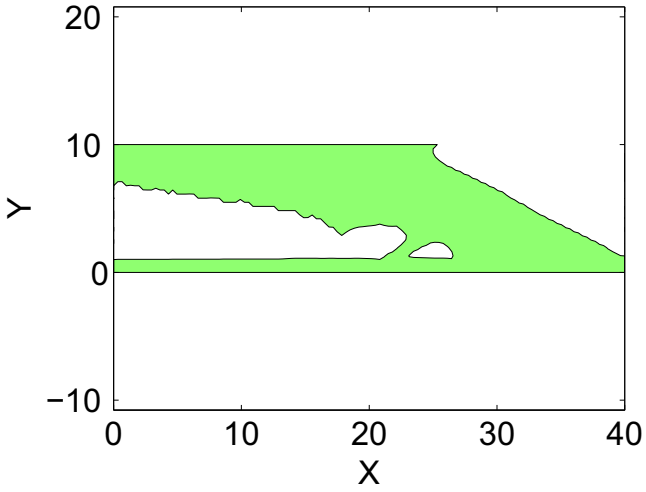

Fig. 3. Optimal topology for maximizing the ECF of a ZnO nanobeam of dimensions 40 × 10 nm. Note that the substrate is not shown.

10 nm nanobeam for both open and closed circuit boundary conditions. The 40 × 10 nm beam was meshed with 120 × 30 Q4 elements, respectively. We note that a significant amount of material is removed from the region where the mechanical force is applied, along with the region where the beam is clamped, as shown in Fig. 3.

To explain the optimized structure that is obtained in Fig. 3, we first note that the piezoelectric layer lies above the neutral axis of the piezoelectric layer/substrate composite beam. Material is removed from the interior of the beam (i.e. between $x=0$ and $x=20$ nm in Fig. 3) rather than at the surface because the stresses and strains in the beam are largest at the surfaces, and not in the beam interior. Similarly, material close to the free end at $x=40$ nm is relatively unstrained and thus can also be removed in the optimization.

The distribution of the material in the optimized beams also has a direct connection to the energy harvesting potential. Specifically, the nanobeam in Fig. 3 is only subject to mechanical loads, and so any electrical energy that is generated can only be due to the piezoelectric coupling constants. Material that is relatively unstrained is not needed for the mechanical integrity, and also contributes little to the generation of electrical energy. As the remaining material in the optimized structure is needed to resist mechanical loading, and is more highly strained, these regions will have larger electrical displacements, and thus conversion of mechanical to electrical energy, leading to increased EMCC.

Tables 3 and 4 show the nominal EMCC obtained for various geometries and aspect ratios considered for both open and closed circuit electrical boundary conditions, where the nominal EMCC is the ratio of the EMCC of the optimal topology with surface effects and the EMCC of the solid beam with surface effects. Different thicknesses were chosen to illustrate the size-dependent nature of the surface effects. There are several noticeable and interesting trends, which we now discuss.

The first effect is that, for both open and closed circuit boundary conditions as shown in Tables 3 and 4, the nominal EMCC decreases with increasing nanobeam thickness. In all cases the optimized EMCC is greater than one. This is because the inclusion of surface piezoelectric effects can only lead to an increase in the energy conversion for a solid ZnO nanobeam because the bulk and surface coupling constants e_{31} and e_{31}^{s} have the same sign (Hoang et al., 2013), though the increase in energy conversion decreases with increasing nanobeam thickness.

In the optimal topology obtained, both surface piezoelectric and surface elastic effects compete to influence the energy conversion, as illustrated in Table 5 for the 40 × 10 nm nanobeam under the open circuit boundary condition, where we note that the following findings are also valid for the closed circuit boundary condition. To delineate these effects, we considered different combinations of including or neglecting surface piezoelectric and elastic effects via the corresponding

Table 3
Nominal EMCC of optimized piezoelectric nanobeam under open circuit conditions.

Nanobeam dimensions (nm)	Nominal EMCC ($C^s \neq 0$, $e^s \neq 0$)
Aspect ratio=4	
40 × 10	1.18
80 × 20	1.12
160 × 40	1.09
Aspect ratio=8	
80 × 10	1.15
160 × 20	1.085
240 × 30	1.06

Table 4
Nominal EMCC of optimized piezoelectric nanobeam under closed circuit condition.

Nanobeam dimensions (nm)	Nominal EMCC ($C^s \neq 0$, $e^s \neq 0$)
Aspect ratio=4	
40 × 10	2.3
80 × 20	2.05
160 × 40	1.9
Aspect ratio=8	
80 × 10	2.35
160 × 20	2.1
240 × 30	2.0

Table 5
The mechanical and electrical energy values under open circuit boundary conditions for the 40 × 10 nm optimized beam shown in Fig. 3.

Different cases	Electrical energy (nJ)	Mechanical energy (nJ)	EMCC	Nominal EMCC
$C_s=0$, $e_s \neq 0$	0.67	6.69	0.091	1.39
$C_s \neq 0$, $e_s \neq 0$	0.534	6.3	0.0781	1.19
$C_s \neq 0$, $e_s = 0$	0.442	6.47	0.064	0.97
$C_s=0$, $e_s=0$	0.543	6.924	0.0727	1.1

surface elastic or piezoelectric stiffness tensors. As shown in Table 5, when surface elastic constants are ignored ($C_s = 0$), the nominal EMCC increases. If only surface elasticity is considered, both the mechanical and electrical energies are smaller than the no surface effects case ($C_s = 0$, $e_s = 0$), leading to a nominal EMCC of less than one. This is because the presence of surface elasticity increases the beam stiffness, which results in a decrease in strain. This decrease in strain reduces the resulting electrical energy to 0.442 nJ, which is the smallest among all cases shown in Table 5. For the purely surface piezoelectric case, the electrical energy is the largest among all the cases leading to the highest nominal EMCC. This parametric study demonstrates that surface elastic effects in ZnO act to reduce the energy conversion ability of the nanobeams while the surface piezoelectric effects enhance the energy conversion ability.

The second effect is that the nominal EMCC is substantially higher for the closed circuit boundary condition, which corresponds to the flow of current across the nanobeam cross section, as compared to the open circuit boundary condition, which corresponds to a build up of voltage across the nanobeam cross section. In the closed circuit condition, the potentials at the top and bottom surfaces of the piezoelectric layer are constrained to zero. However, during the optimization process, new surfaces are formed inside the beam. These new surfaces are not constrained to zero potential, which enables the EMCC for the closed circuit boundary condition to approach the open circuit value after optimization. This can also be observed by looking at the distribution of potential across the solid 40 × 10 nm beam at $x=10$ nm as shown in Fig. 4(a) under open and closed circuit conditions. As can be seen in Fig. 4(a) for the solid beam with surface effects, the potential difference between the electrodes on the top and bottom surfaces is about 3 V for open circuit, but zero for closed circuit.

In contrast, the potential distribution is similar for both open and closed circuit conditions after optimization, as shown in Fig. 4(b). In Fig. 3, it can be seen at $x=10$ nm, there is material present from $y=0$ to 1.3 nm, and then no material between $y=1.3$ and 5.35 nm, which is the location of two newly formed free surfaces at $x=10$. In Fig. 4(b), it is shown that the potential difference between $y=0$ and 1.3 nm is 0.34 V while the potential difference between $y=5.35$ nm and $y=10$ nm is around 2.85 V for both open and closed circuit conditions. Furthermore, the EMCC of the optimal 40 × 10 nm beam under closed circuit condition is 0.078, while under open circuit condition the EMCC is 0.0785, thus showing that as the potential distribution of open and closed circuit becomes similar for the optimal topology, the EMCC under closed circuit approaches the EMCC under open circuit condition. The EMCC of the solid 40 × 10 nm beam under closed circuit condition is 0.034 while under open circuit condition the EMCC is 0.067, which yields a nominal EMCC under open circuit condition of $\frac{0.0785}{0.067} = 1.18$, while under closed circuit condition, the nominal EMCC is $\frac{0.078}{0.034} = 2.3$. Therefore due to the appearance of new free surfaces in the optimal topology, the nominal EMCC under closed circuit condition is higher compared to the one under open circuit condition.

5.2. Three-dimensional piezoelectric nanoplate

In this section, we examine the piezoelectric behavior of a three-dimensional ZnO nanoplate on substrate, as illustrated in Fig. 5. We refer to this system as an energy harvesting device (EHD) in the following discussion. This particular geometry was chosen because while the two-dimensional nanobeam geometry studied previously is simple, manufacturing the

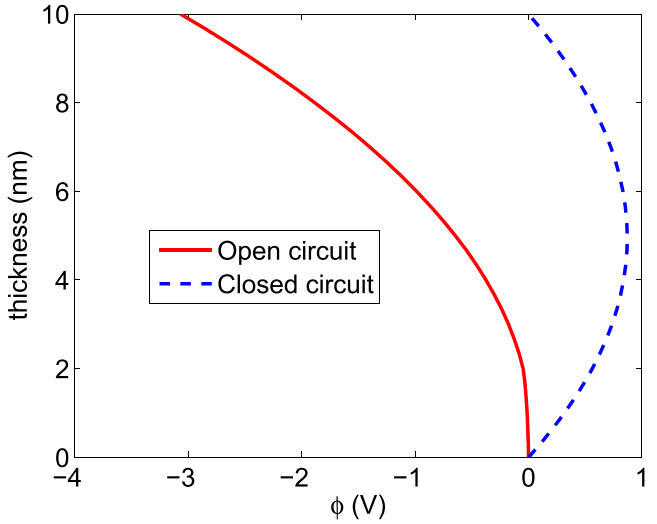

(a)

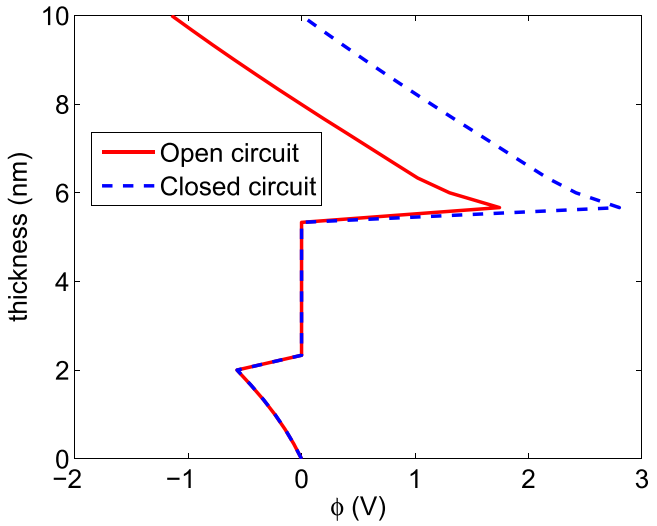

(b)

Fig. 4. Electrical potential distribution across the thickness of the 40 × 10 nm, (a) solid beam and (b) optimal beam from Fig. 3, at $x = 10$ nm.

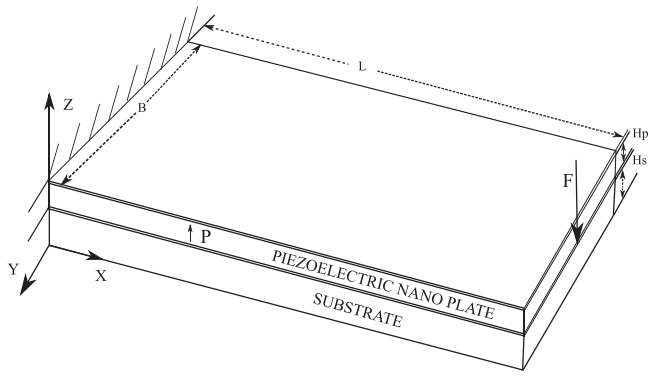

Fig. 5. A piezoelectric ZnO nanoplate on substrate subjected to point load, F at free end, with P indicating the poling direction.

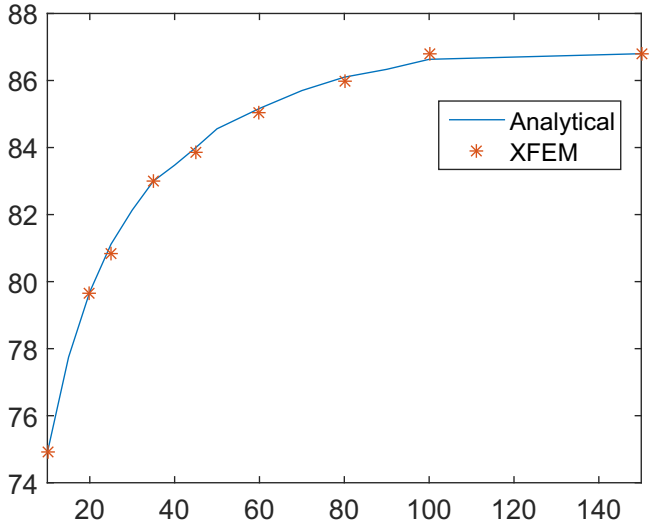

Fig. 6. Variation of dimensionless maximum deflection with depth of plate.

complex shapes that emerge from the topology optimization may pose significant challenges, particularly with a beam thickness of around 10 nm. In this example, the thickness of the nano plate is fixed while the in-plane topology of the nano plate is altered. Thus, the holes that are formed through the thickness, which have feature sizes larger than tens of nanometers, could likely be lithographically manufactured using technology that is available today.

5.2.1. Finite element model validation

An analytic expression for the deflection of a piezoelectric nanoplate including surface piezoelectric and elastic effects based on Kirchoff plate theory was recently given by Wang (2012) as

$$w(x,y) = \sum_{m=1}^{\infty}\sum_{n=1}^{\infty} A_{mn}\sin\left(\frac{m\pi x}{a}\right)\sin\left(\frac{n\pi y}{b}\right) \tag{55}$$

where

$$A_{mn} = \frac{16q}{mn\pi^2 Y} \tag{56}$$

$$Y = \left[\left(\tilde{c}_{11} + \frac{\tilde{e}_{31}^2}{\tilde{\kappa}_{33}}\right)\frac{h^3}{12} + \left(c_{11}^s + \frac{e_{31}^s\tilde{e}_{31}}{\tilde{\kappa}_{33}}\right)\frac{h^2}{2}\right]X\left[\left(\frac{m\pi}{a}\right)^4 + \left(\frac{n\pi}{b}\right)^4\right] + \left[\left(\tilde{c}_{12} + \frac{\tilde{e}_{31}^2}{\tilde{\kappa}_{33}}\right)\frac{h^3}{6} + \left(2c_{66}^s + c_{12}^s + \frac{e_{31}^s\tilde{e}_{31}}{\tilde{\kappa}_{33}}\right)h^2\right]X\left(\frac{m^2n^2\pi^4}{a^2b^2}\right) \tag{57}$$

q refers to uniformly distributed load over the plate; $\tilde{c}_{11} = c_{11} - \frac{c_{13}^2}{c_{33}}$, $\tilde{c}_{12} = c_{12} - \frac{c_{13}^2}{c_{33}}$, $\tilde{e}_{31} = e_{31} - \frac{c_{13}e_{33}}{c_{33}}$. $\tilde{\kappa}_{33} = \kappa_{33} - \frac{e_{33}^2}{c_{33}}$ and m, $n = 1,3,5\ \ldots$

The FE model of the piezoelectric nano plate is performed by an equivalent 2D model as discussed in Appendix C.

The approximation of the electric potential field is made by discretizing the plate into several sublayers with linear variation of electric potential within each sublayer (Wang, 2004). The number of sublayers for electric potential discretizaton is taken to be 10. The piezoelectric plate considered in this example is poled vertically along the z-direction as shown in Fig. 5. Fig. 6 shows good agreement between the analytic and FE solutions, where the dimensions of the nano plate were 200 × 50 nm for the length and width, while the depth was varied from 10 to 100 nm.

5.2.2. Optimization of piezoelectric nanoplate layer

The EHD is composed of a substrate and a piezoelectric ZnO nanoplate, as shown in Fig. 5. The substrate is assumed to be made of aluminum, and the thickness of the substrate, H_s and the piezoelectric layer, H_p are taken to be 125 nm and 100 nm respectively. The length and width of this EHD is assumed to be 4×2 μm. Two electrical boundary conditions are

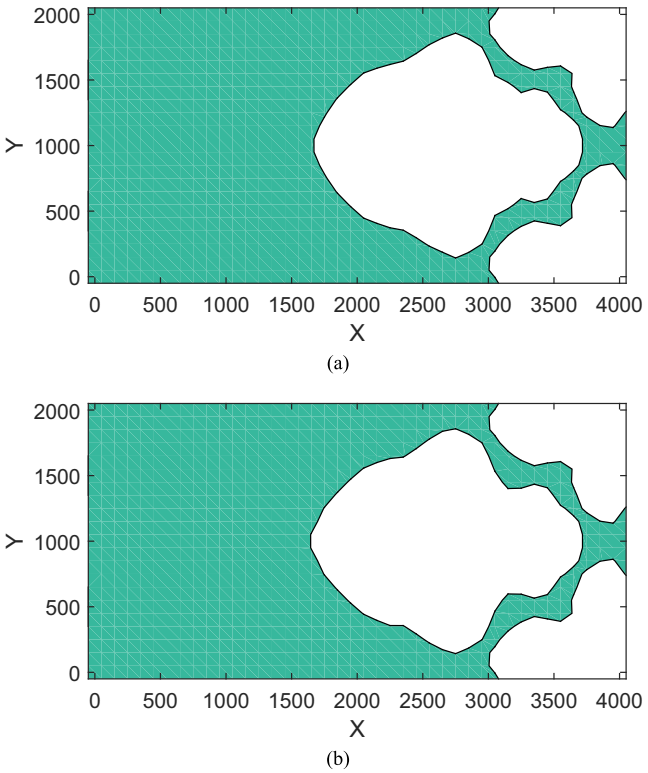

Fig. 7. Optimized topology (top view) of the piezoelectric layer (top view) of an EHD subjected to point load at free end. (a) 100 nm thick nanoplate; (b) 10 nm thick nanoplate. Same optimized topology obtained for both open and closed circuit boundary conditions.

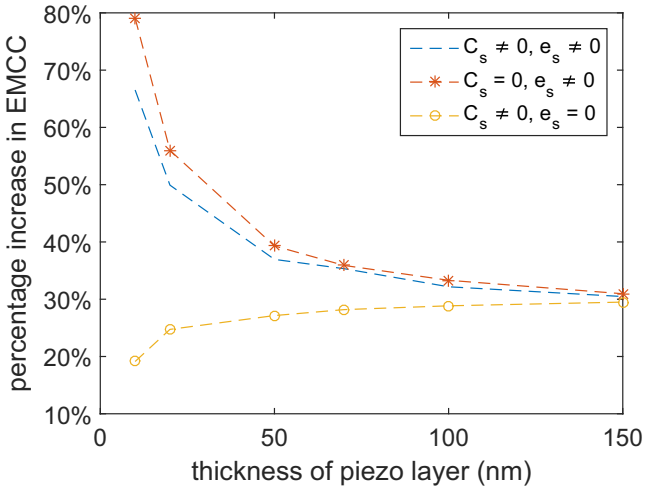

Fig. 8. The percentage increase in EMCC with varying thickness of the piezoelectric nanoplate under closed circuit boundary conditions.

considered, with electrodes on the top of the nanoplate and underneath the substrate. In closed circuit boundary condition, both the top and bottom electrodes are grounded. In open circuit boundary condition, only the bottom electrode is grounded.

We then optimize the geometry of the piezoelectric nanoplate to maximize the EMCC of the EHD, while the geometry and shape of the substrate remain unchanged. The optimized topology of the 100 nm thick piezoelectric nanoplate is shown in Fig. 7(a) for both open and closed circuit boundary conditions. The nominal EMCC of this optimized EHD is 1.31 and 1.32 under closed and open circuit boundary conditions, respectively.

Table 6
Comparison of nominal EMCC between solid and optimized piezoelectric nanoplate of dimension 4000 × 2000 × 10 nm under open circuit condition in an EHD.

	Solid piezoelectric nanoplate, Fig. 9(a)	Trial topology, Fig. 9(b)	Optimized piezoelectric nanoplate, Fig. 7(b)
Volume fraction	1	0.6	0.6
Π_e (nJ)	2.23	3.15	2.48
Π_d (nJ)	0.12	0.13	0.17
EMCC	0.05	0.04	0.064
Nominal EMCC	1	0.8	1.28

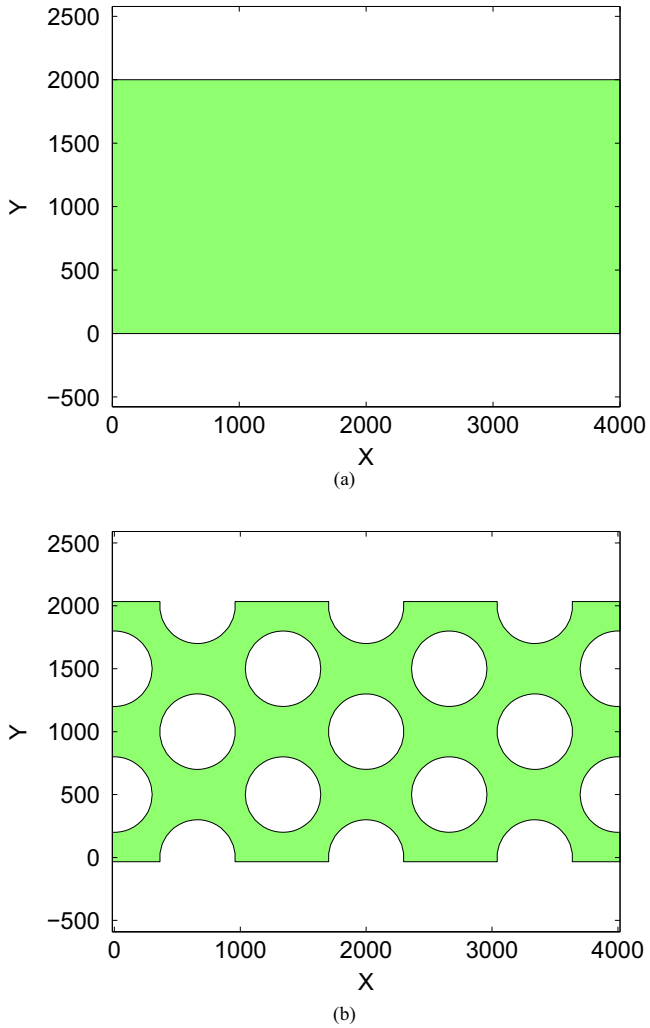

Fig. 9. Top view of (a) solid nanoplate and (b) a random optimal topology under open circuit boundary conditions. The thickness of the nanoplate is 10 nm.

To examine size effects on the EMCC and optimized topology, we studied the effect of replacing the 100 nm nanoplate with a 10 nm thick nanoplate, with the optimized topology for the 10 nm nanoplate shown in Fig. 7(b). The optimum topologies are similar to those seen previously for the two-dimensional nanobeam, in that some material around the point force is removed, along with a section of the nanobeam away from the loading surface. The nominal EMCC of the optimized EHD for 10 nm thick piezoelectric layer is 1.29 and 1.28 under closed and open circuit conditions respectively. The optimized topology and the nominal EMCC for the 100 nm and 10 nm piezoelectric layers remain similar. This shows that, at least for the nanoplate geometry, the presence of surface effects does not influence the optimum topology for the maximum energy conversion objective function.

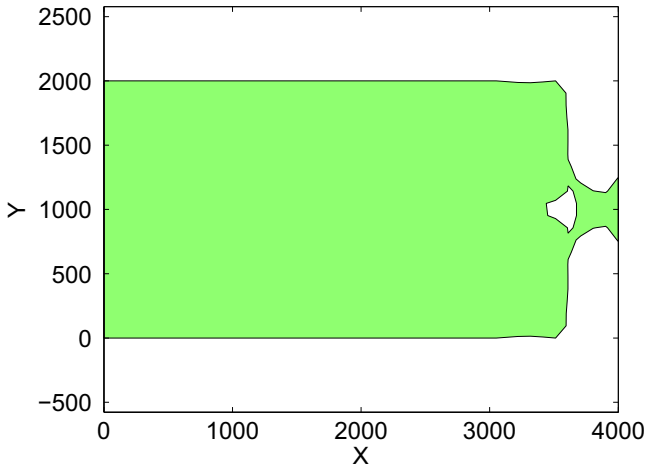

Fig. 10. Top view of the optimal topology for the maximum energy conversion objective function with a constraint on the increase in EMCC. The thickness of the nanoplate is 10 nm.

While the optimal topology may not change substantially, surface effects and optimization combine to significantly increase the energy harvesting capability of piezoelectric nanoplates. For example, the ratio of the EMCC of a 100 nm thick nanoplate with surface effects to the EMCC of a 100 nm nanoplate ignoring surface effects is 1.03 and 1.01 under closed and open circuit conditions respectively. However, the EMCC after optimization is 0.0163 and 0.059 under closed and open circuit conditions, resulting in an increase of 32% and 29% under closed and open circuit boundary conditions respectively. Furthermore, the ratio of the EMCC of a 10 nm thick nanoplate with surface effects to the EMCC of a 10 nm thick nanoplate ignoring surface effects is 1.39 and 1.18 under closed and open circuit conditions respectively. However, with optimization and surface effects, the EMCC is 0.021 and 0.067 for closed and open circuit conditions, leading to a combined increase in EMCC due to optimization and surface effects of 68% and 46%, respectively.

Fig. 8 shows the change in the EMCC as a function of the thickness of the piezoelectric nanoplate under closed circuit conditions. Similar, but slightly smaller increases are seen for open circuit conditions. The figure shows the interaction between surface elastic and surface piezoelectric effects in controlling the energy conversion of the EHD. With decrease in thickness of the nanoplate, the surface elastic effects increase the stiffness of the plate and thus the mechanical energy, leading to reduction in energy conversion. In contrast, the surface piezoelectric effects enhance the coupling ability leading to an increase in energy conversion of the EHD overcoming the reduction caused by the surface elastic effects. It can also be seen from the figure that for the case $C_s = 0$; $e_s \neq 0$ the energy conversion is a maximum. This is because under this case, there is only an increase in piezoelectric coupling and no increase in stiffness of the plate with decreasing thickness.

Table 6 shows the mechanical energy, electrical energy and EMCC for a solid piezoelectric nanoplate from Fig. 9(a), a random optimal topology in Fig. 9(b), and the calculated optimal topology from Fig. 7(b) under open circuit conditions. As shown in Table 6, though there is a slight increase in mechanical strain energy from reducing the volume fraction, there is a significant increase in electrical energy as material gets distributed to the optimal topology shown in Fig. 7(b). From Table 6, it is also clear that for the same volume fraction as the optimum topology, random removal of material like the one shown in Fig. 9(b) results in a considerable increase in mechanical strain energy with only a modest increase in electrical energy, leading to a reduction in the EMCC.

Finally, while surface effects may not significantly alter the optimum geometry as the nanoplate becomes thinner, they do have a significant effect on the efficiency of the energy conversion. Fig. 10 shows the optimum topology for a 10 nm thick piezoelectric nanoplate if the increase in EMCC is constrained to 32% and 29% for open and closed circuit conditions respectively. These values are the maximum increase in EMCC obtained for a 100 nm thick piezoelectric nanoplate. The volume fraction of the optimum topology shown in Fig. 10 is 0.93, whereas the volume fraction of the topology for the 100 nm thick nanoplate obtained for the same increase in energy conversion shown in Fig. 7(a) is 0.6. Fig. 10 demonstrates that the same increase in EMCC can be obtained with significantly less removal of material in smaller piezoelectric nanoplates due to the increasing importance and impact of surface piezoelectric effects for decreasing nanostructure size.

6. Conclusion

In conclusion, we have formulated and presented a new extended finite element model that is coupled to topology optimization to study the energy harvesting potential of piezoelectric nanostructures. Our simulations have demonstrated the improvements in energy conversion efficiency that can be realized due to a combination of surface effects and topology optimization. We have also elucidated the competition between surface elastic and surface piezoelectric effects in controlling the overall energy conversion efficiency of the piezoelectric nanostructures.

Appendix A. Derivation of adjoint problem

The objective function and its constraints are as follows:
Minimize

$$\text{Minimize} \quad J(\Psi) = \frac{1}{k^2} = \frac{\Pi_e}{\Pi_d} \tag{A.1}$$

$$\text{Subject to} \quad \int_\Omega d\Omega - \bar{V} = 0 \tag{A.2}$$

$$a(\mathbf{u}, \boldsymbol{\phi}, \delta\mathbf{u}, \delta\boldsymbol{\phi}) + a_s(\mathbf{u}, \boldsymbol{\phi}, \delta\mathbf{u}, \delta\boldsymbol{\phi}) = -l_s(\delta\mathbf{u}, \delta\boldsymbol{\phi}) + l(\delta\mathbf{u}, \delta\boldsymbol{\phi}) \tag{A.3}$$

$$\begin{aligned}
\dot{a}(\mathbf{u}, \boldsymbol{\phi}, \mathbf{w}, \boldsymbol{\psi}) = {} & \int_\Omega \boldsymbol{\epsilon}^T(\mathbf{u}'): \mathbb{C}^{bulk}: \boldsymbol{\epsilon}(\mathbf{w})\, d\Omega + \int_\Omega \boldsymbol{\epsilon}^T(\mathbf{u}): \mathbb{C}^{bulk}: \boldsymbol{\epsilon}(\mathbf{w}')\, d\Omega + - \int_\Omega \boldsymbol{\epsilon}(\boldsymbol{u}')^T: \boldsymbol{e}^T{\cdot}\boldsymbol{E}(\boldsymbol{\psi})\, d\Omega \\
& - \int_\Omega \boldsymbol{\epsilon}(\boldsymbol{u})^T: \boldsymbol{e}^T{\cdot}\boldsymbol{E}(\boldsymbol{\psi}')\, d\Omega - \int_\Gamma \boldsymbol{\epsilon}(\boldsymbol{u})^T: \boldsymbol{e}^T{\cdot}\boldsymbol{E}(\boldsymbol{\psi}){\cdot}V_n\, d\Gamma \int_\Gamma \boldsymbol{\epsilon}^T(\mathbf{u}): \mathbb{C}^{bulk}: \boldsymbol{\epsilon}(\mathbf{w}){\cdot}V_n\, d\Gamma \\
& - \int_\Omega \boldsymbol{E}(\boldsymbol{\phi}')^T{\cdot}\boldsymbol{e}^{bulk}: \boldsymbol{\epsilon}(\mathbf{w})\, d\Omega - \int_\Omega \boldsymbol{E}(\boldsymbol{\phi})^T{\cdot}\boldsymbol{e}^{bulk}: \boldsymbol{\epsilon}(\mathbf{w}')\, d\Omega - \int_\Gamma \boldsymbol{E}(\boldsymbol{\phi})^T{\cdot}\boldsymbol{e}^{bulk}: \boldsymbol{\epsilon}(\mathbf{w}){\cdot}V_n\, d\Gamma \\
& - \int_\Omega \boldsymbol{E}(\boldsymbol{\phi}')^T{\cdot}\boldsymbol{\kappa}{\cdot}\boldsymbol{E}(\boldsymbol{\psi})\, d\Omega - \int_\Omega \boldsymbol{E}(\boldsymbol{\phi})^T{\cdot}\boldsymbol{\kappa}{\cdot}\boldsymbol{E}(\boldsymbol{\psi}')\, d\Omega - \int_\Gamma \boldsymbol{E}(\boldsymbol{\phi})^T{\cdot}\boldsymbol{\kappa}{\cdot}\boldsymbol{E}(\boldsymbol{\psi}){\cdot}V_n\, d\Gamma
\end{aligned} \tag{A.4}$$

$$\begin{aligned}
\dot{a}_s(\mathbf{u}, \boldsymbol{\phi}, \mathbf{w}, \boldsymbol{\psi}) = {} & \int_\Gamma \boldsymbol{\epsilon}_{\boldsymbol{s}}(\mathbf{u}')^T: \boldsymbol{C}_{\boldsymbol{s}}: \boldsymbol{\epsilon}_{\boldsymbol{s}}(\boldsymbol{w})\, d\Gamma + \int_\Gamma \boldsymbol{\epsilon}_{\boldsymbol{s}}(\boldsymbol{u})^T: \boldsymbol{C}_{\boldsymbol{s}}: \boldsymbol{\epsilon}_{\boldsymbol{s}}(\boldsymbol{w}')\, d\Gamma \\
& + \int_\Gamma [\nabla(\boldsymbol{\epsilon}_{\boldsymbol{s}}(\boldsymbol{u}): \boldsymbol{C}_{\boldsymbol{s}}: \boldsymbol{\epsilon}_{\boldsymbol{s}}(\boldsymbol{w}))\cdot n + (\boldsymbol{\epsilon}_{\boldsymbol{s}}(\boldsymbol{u}): \boldsymbol{C}_{\boldsymbol{s}}: \boldsymbol{\epsilon}_{\boldsymbol{s}}(\boldsymbol{w}))\cdot\eta]{\cdot}V_n\, d\Gamma - \int_\Gamma \boldsymbol{\epsilon}_{\boldsymbol{s}}(\boldsymbol{u}')^T: \boldsymbol{e}_{\boldsymbol{s}}^T{\cdot}\boldsymbol{E}_{\boldsymbol{s}}(\boldsymbol{\psi})\, d\Gamma \\
& - \int_\Gamma \boldsymbol{\epsilon}_{\boldsymbol{s}}(\boldsymbol{u})^T: \boldsymbol{e}_{\boldsymbol{s}}^T{\cdot}\boldsymbol{E}_{\boldsymbol{s}}(\boldsymbol{\psi}')\, d\Gamma \int_\Gamma [\nabla(\boldsymbol{\epsilon}_{\boldsymbol{s}}(\boldsymbol{u})^T: \boldsymbol{e}_{\boldsymbol{s}}^T{\cdot}E_s(\boldsymbol{\psi})))\cdot n + (\boldsymbol{\epsilon}_{\boldsymbol{s}}(\boldsymbol{u})^T: \boldsymbol{e}_{\boldsymbol{s}}^T{\cdot}\boldsymbol{E}_{\boldsymbol{s}}(\boldsymbol{\psi}))\eta]{\cdot}V_n\, d\Gamma \\
& - \int_\Gamma \boldsymbol{E}_{\boldsymbol{s}}(\boldsymbol{\phi}')^T{\cdot}\boldsymbol{e}_{\boldsymbol{s}}: \boldsymbol{\epsilon}_{\boldsymbol{s}}(\boldsymbol{w})\, d\Gamma - \int_\Gamma \boldsymbol{E}_{\boldsymbol{s}}(\boldsymbol{\phi})^T{\cdot}\boldsymbol{e}_{\boldsymbol{s}}: \boldsymbol{\epsilon}_{\boldsymbol{s}}(\boldsymbol{w}')\, d\Gamma \\
& - \int_\Gamma [\nabla(\boldsymbol{E}_{\boldsymbol{s}}(\boldsymbol{\phi})^T{\cdot}\boldsymbol{e}_{\boldsymbol{s}}: \boldsymbol{\epsilon}(\boldsymbol{w}))\cdot n + (\boldsymbol{E}_{\boldsymbol{s}}(\boldsymbol{\phi})^T{\cdot}\boldsymbol{e}_{\boldsymbol{s}}: \boldsymbol{\epsilon}(\boldsymbol{w}))\eta]{\cdot}V_n\, d\Gamma \\
& - \int_\Gamma \boldsymbol{E}_{\boldsymbol{s}}(\boldsymbol{\phi}')^T{\cdot}\boldsymbol{\kappa}_{\boldsymbol{s}}{\cdot}\boldsymbol{E}_{\boldsymbol{s}}\boldsymbol{\psi}\, d\Gamma - \int_\Gamma \boldsymbol{E}_{\boldsymbol{s}}(\boldsymbol{\phi})^T{\cdot}\boldsymbol{\kappa}_{\boldsymbol{s}}{\cdot}\boldsymbol{E}_{\boldsymbol{s}}(\boldsymbol{\psi}')\, d\Gamma - \int_\Gamma [\nabla(\boldsymbol{E}_{\boldsymbol{s}}(\boldsymbol{\phi})^T{\cdot}\boldsymbol{\kappa}_{\boldsymbol{s}}{\cdot}\boldsymbol{E}_{\boldsymbol{s}}(\boldsymbol{\psi})\cdot n + (\boldsymbol{E}_{\boldsymbol{s}}(\boldsymbol{\phi})^T{\cdot}\boldsymbol{\kappa}_{\boldsymbol{s}}{\cdot}\boldsymbol{E}_{\boldsymbol{s}}(\boldsymbol{\psi}))\cdot\eta]\ V_n\, d\Gamma
\end{aligned} \tag{A.5}$$

$$\dot{l}_s(\mathbf{w}) = \int_\Gamma \boldsymbol{\epsilon}_S(\mathbf{w}')\mathbf{P}: \boldsymbol{\tau}_{\mathbf{s}}\, d\Gamma + \int_\Gamma (\nabla_s(\boldsymbol{\epsilon}_S(\mathbf{w}): \boldsymbol{\tau}_{\mathbf{s}})\cdot\mathbf{n} + \eta(\boldsymbol{\epsilon}_S(\mathbf{w}): \boldsymbol{\tau}_{\mathbf{s}}))V_n\, d\Gamma \tag{A.6}$$

$$\dot{l}(\mathbf{w}) = \int_\Omega \mathbf{w}'{\cdot}\mathbf{b}\, d\Omega + \int_\Gamma \mathbf{w}{\cdot}\mathbf{b}\, V_n\, d\Gamma + \int_{\Gamma_N} \mathbf{w}'{\cdot}\mathbf{t}\, d\Gamma + \int_{\Gamma_N} (\nabla(\mathbf{w}{\cdot}\mathbf{t})\cdot\mathbf{n} + \eta\mathbf{w}{\cdot}\mathbf{t})V_n\, d\Gamma \tag{A.7}$$

The Lagrangian of the objective functional is

$$L = J + l(\mathbf{w}) - a(\mathbf{u}, \boldsymbol{\phi}, \mathbf{w}, \boldsymbol{\psi}) - a_s(\mathbf{u}, \boldsymbol{\phi}, \mathbf{w}, \boldsymbol{\psi}) - l_s(\mathbf{w}). \tag{A.8}$$

The material derivative of the Lagrangian is defined as

$$\dot{L} = \dot{J} + \dot{l}(\mathbf{w}) - \dot{a}(\mathbf{u}, \boldsymbol{\phi}, \mathbf{w}, \boldsymbol{\psi}) - \dot{a}_s(\mathbf{u}, \boldsymbol{\phi}, \mathbf{w}, \boldsymbol{\psi}) - \dot{l}_s(\mathbf{w}). \tag{A.9}$$

All the terms that contain $\mathbf{u}'$ and $\boldsymbol{\phi}'$ in the material derivative of Lagrangian are collected and the sum of these terms is set to zero, to get the weak form of the adjoint equation,

$$\int_{\Omega} \boldsymbol{\epsilon}^T(\mathbf{u}^{\prime})\colon \mathbb{C}^{bulk}\colon \boldsymbol{\epsilon}(\mathbf{w})\, d\Omega - \int_{\Omega} \boldsymbol{\epsilon}(\mathbf{u}^{\prime})^T\colon \boldsymbol{e}^T\cdot\boldsymbol{E}(\boldsymbol{\psi})\, d\Omega - \int_{\Gamma} \boldsymbol{\epsilon}_{\boldsymbol{s}}(\mathbf{u}^{\prime})^T\colon \mathbf{C}_{\boldsymbol{s}}\colon \boldsymbol{\epsilon}_{\boldsymbol{s}}(\boldsymbol{w})\, d\Gamma - \int_{\Gamma} \boldsymbol{\epsilon}_{\boldsymbol{s}}(\mathbf{u}^{\prime})^T\colon \boldsymbol{e}_{\boldsymbol{s}}^T\cdot\boldsymbol{E}_{\boldsymbol{s}}(\boldsymbol{\psi})\, d\Gamma = \int_{\Omega} 2C_1\, \boldsymbol{\epsilon}(\mathbf{u}^{\prime})^T\colon \mathbb{C}^{bulk}\colon \boldsymbol{\epsilon}(\boldsymbol{u})\, d\Omega \tag{A.10}$$

$$\int_{\Omega} \boldsymbol{E}(\boldsymbol{\phi}^{\prime})^T\cdot\boldsymbol{e}^{bulk}\colon \boldsymbol{\epsilon}(\mathbf{w})\, d\Omega - \int_{\Omega} \boldsymbol{E}(\boldsymbol{\phi}^{\prime})^T\cdot\boldsymbol{\kappa}\cdot\boldsymbol{E}(\boldsymbol{\psi})\, d\Omega - \int_{\Gamma} \boldsymbol{E}_{\boldsymbol{s}}(\boldsymbol{\phi}^{\prime})^T\cdot\boldsymbol{e}_{\boldsymbol{s}}\colon \boldsymbol{\epsilon}_{\boldsymbol{s}}(\boldsymbol{w})\, d\Gamma - \int_{\Gamma} \boldsymbol{E}_{\boldsymbol{s}}(\boldsymbol{\phi}^{\prime})^T\cdot\boldsymbol{\kappa}_{\boldsymbol{s}}\cdot\boldsymbol{E}_{\boldsymbol{s}}\boldsymbol{\psi}\, d\Gamma = \int_{\Omega} 2C_2\, \boldsymbol{E}(\boldsymbol{\phi}^{\prime})^T\cdot\boldsymbol{\kappa}\cdot\boldsymbol{E}(\boldsymbol{\phi})\, d\Omega \tag{A.11}$$

Appendix B. Bulk and surface stiffness matrices

The bulk and surface stiffness matrices corresponding to the discrete finite element equations in Eq. (24) are defined as follows:

$$\begin{aligned} \boldsymbol{K}_{\boldsymbol{uu}}^{\boldsymbol{b}} &= \int_{\Omega} \boldsymbol{B}_{\boldsymbol{u}}^{\boldsymbol{T}}\{\mathbb{C}\}\boldsymbol{B}_{\boldsymbol{u}}\, d\Omega \\ \boldsymbol{K}_{\boldsymbol{uu}}^{\boldsymbol{s}} &= \int_{\Gamma} \boldsymbol{B}_{\boldsymbol{u}}^{\boldsymbol{T}}\boldsymbol{M}_{\boldsymbol{p}}^{\boldsymbol{T}}\{\mathbb{C}^{s}\}\boldsymbol{M}_{\boldsymbol{p}}\boldsymbol{B}_{\boldsymbol{u}}\, d\Gamma \end{aligned} \tag{B.1}$$

$$\begin{aligned} \boldsymbol{K}_{\boldsymbol{\phi u}}^{\boldsymbol{b}} &= \int_{\Omega} \boldsymbol{B}_{\boldsymbol{\phi}}^{T}\{\mathbf{e}\}\boldsymbol{B}_{\boldsymbol{u}}\, d\Omega \\ \boldsymbol{K}_{\boldsymbol{\phi u}}^{\boldsymbol{s}} &= \int_{\Gamma} \boldsymbol{B}_{\boldsymbol{\phi}}^{T}\boldsymbol{P}_{\boldsymbol{\phi}}^{\boldsymbol{T}}\{\mathbf{e}_{\mathbf{s}}\}\boldsymbol{M}_{\boldsymbol{p}}\boldsymbol{B}_{\boldsymbol{u}}\, d\Gamma \end{aligned} \tag{B.2}$$

$$\boldsymbol{K}_{\boldsymbol{u\phi}}^{\boldsymbol{b}} = \int_{\Omega} \boldsymbol{B}_{\boldsymbol{u}}^{T}\{\mathbf{e}\}^{T}\boldsymbol{B}_{\boldsymbol{\phi}}\, d\Omega$$

$$\boldsymbol{K}_{\boldsymbol{u\phi}}^{\boldsymbol{s}} = \int_{\Gamma} \boldsymbol{B}_{\boldsymbol{u}}^{T}\boldsymbol{M}_{\boldsymbol{P}}^{\boldsymbol{T}}\{\mathbf{e}_{\mathbf{s}}\}^{T}\boldsymbol{P}_{\boldsymbol{\phi}}\boldsymbol{B}_{\boldsymbol{\phi}}\, d\Gamma \tag{B.3}$$

$$\begin{aligned} \boldsymbol{K}_{\boldsymbol{\phi\phi}}^{\boldsymbol{b}} &= -\int_{\Omega} \boldsymbol{B}_{\boldsymbol{\phi}}^{T}\{\boldsymbol{\kappa}\}\boldsymbol{B}_{\boldsymbol{\phi}}\, d\Omega \\ \boldsymbol{K}_{\boldsymbol{\phi\phi}}^{\boldsymbol{s}} &= -\int_{\Gamma} \boldsymbol{B}_{\boldsymbol{\phi}}^{T}\boldsymbol{P}^{\boldsymbol{T}}\{\boldsymbol{\kappa}_{\boldsymbol{s}}\}\boldsymbol{P}\boldsymbol{B}_{\boldsymbol{\phi}}\, d\Gamma \end{aligned} \tag{B.4}$$

$$\begin{aligned} \boldsymbol{f}_{\boldsymbol{u}}^{\boldsymbol{s}} &= \int_{\Gamma} \boldsymbol{B}_{\boldsymbol{u}}^{\boldsymbol{T}}\boldsymbol{M}_{\boldsymbol{p}}^{\boldsymbol{T}}\boldsymbol{\tau}_{\boldsymbol{s}}\, d\Gamma \\ \boldsymbol{f}_{\boldsymbol{u}}^{\boldsymbol{ext}} &= \int_{\Gamma_N} \boldsymbol{N}^{\boldsymbol{T}}\bar{\mathbf{t}}\, d\Gamma + \int_{\Omega} \boldsymbol{N}^{\boldsymbol{T}}\, \boldsymbol{b}\, d\Omega \\ \boldsymbol{g}_{\boldsymbol{u}}^{\boldsymbol{s}} &= \int_{\Gamma} \boldsymbol{B}_{\boldsymbol{\phi}}^{\boldsymbol{T}}\boldsymbol{P}^{\boldsymbol{T}}\boldsymbol{\omega}_{\boldsymbol{s}}\, d\Gamma \\ \boldsymbol{g}_{\boldsymbol{u}}^{\boldsymbol{ext}} &= -\int_{\Omega} \boldsymbol{N}^{\boldsymbol{T}}\, \boldsymbol{q}\, d\Omega \end{aligned} \tag{B.5}$$

Here $\mathbf{P}$ is the tangential projection tensor to Γ at $\mathbf{x} \in \Gamma$ which is defined as $\mathbf{P}(\mathbf{x}) = \mathbf{I} - \mathbf{n}(\mathbf{x}) \otimes \mathbf{n}(\mathbf{x})$, $\mathbf{I}$ is the second order unit tensor. $\boldsymbol{M_p}$ is defined as

$$\boldsymbol{M_P} = \begin{pmatrix} P_{11}^2 & P_{12}^2 & P_{11}P_{12} \\ P_{12}^2 & P_{22}^2 & P_{12}P_{22} \\ 2P_{11}P_{12} & 2P_{12}P_{22} & P_{12}^2 + P_{11}P_{22} \end{pmatrix} \tag{B.6}$$

The matrices $\boldsymbol{B_u}$ and $\boldsymbol{B_\phi}$ comprise standard FEM and enrichment parts. The $\boldsymbol{B_u}$ and $\boldsymbol{B_\phi}$ matrices are

$$\boldsymbol{B}_{\boldsymbol{u}} = \begin{bmatrix} \boldsymbol{B}_{\boldsymbol{u},\boldsymbol{std}} & \boldsymbol{B}_{\boldsymbol{u},\boldsymbol{enr}} \end{bmatrix}$$

$$\boldsymbol{B}_{\boldsymbol{u},\boldsymbol{std}} = \begin{pmatrix} N_x & 0 \\ 0 & N_y \\ N_y & N_x \end{pmatrix}$$

$$\boldsymbol{B}_{\boldsymbol{u},\boldsymbol{enr}} = \begin{pmatrix} f\,N_x + f,x\,N & 0 \\ 0 & f\,N_y + f,y\,N \\ f\,N_y + f,y\,N & f\,N_x + f,x\,N \end{pmatrix}$$

$$\boldsymbol{B}_{\phi} = \begin{bmatrix} \boldsymbol{B}_{\phi,\boldsymbol{std}} & \boldsymbol{B}_{\phi,\boldsymbol{enr}} \end{bmatrix}$$

$$\boldsymbol{B}_{\phi,\boldsymbol{std}} = \begin{pmatrix} N_x \\ N_y \end{pmatrix}$$

$$\boldsymbol{B}_{\phi,\boldsymbol{enr}} = \begin{pmatrix} f\,N_x + f,x\,N \\ f\,N_y + f,y\,N \end{pmatrix} \tag{B.7}$$

The enrichment f used for modelling weak discontinuity is (Moes et al., 2003)

$$f = \sum_{i\in I} N_i|\Psi_i| - \left|\sum_{i\in I} N_i\Psi_i\right| \tag{B.8}$$

Appendix C. Finite element model of a piezoelectric nanoplate

Piezoelectric energy harvesters are usually thin flexible structures and so Kirchoff plate theory adopted in Junior et al. (2009) is employed in this work. A rectangular finite element with three mechanical degrees of freedom (u, v and w in x, y and z directions) is adopted to model displacements in substructure and nano-piezo layer. The transverse displacement is assumed to vary in polynomial form in an element,

$$w(x) = \boldsymbol{T}\boldsymbol{a} \tag{C.1}$$

where the polynomial terms

$$\boldsymbol{T} = [1\ x\ y\ x^2\ xy\ y^2\ x^3\ x^2y\ xy^2\ y^3\ x^3y\ xy^3] \tag{C.2}$$

$\boldsymbol{a}$ is a vector of generalized coordinates. $w(x)$ in terms of nodal displacements can written as

$$w = \boldsymbol{N}\boldsymbol{W} \tag{C.3}$$

where $\boldsymbol{N} = \boldsymbol{T}\boldsymbol{A}^{-1}$, $\boldsymbol{A}$ is a 12×12 transformation matrix comprising nodal values of $\boldsymbol{T}$ and its derivatives while $\boldsymbol{W}$ is a vector of nodal variables. The vector of curvatures can be expressed as follows:

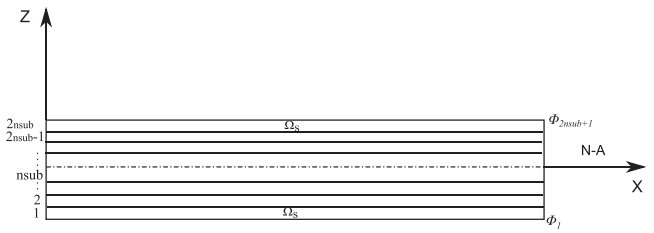

Fig. C1. Discretization for electric potential field with top and bottom layers having surface material properties.

$$\left[\frac{\partial^2 w}{\partial^2 x}\ \frac{\partial^2 w}{\partial^2 y}\ 2\frac{\partial^2 w}{\partial x \partial y}\right]^T = \boldsymbol{B_u W} \tag{C.4}$$

Approximation of electric potential field can be obtained by discretizing the nano-piezoelectric plate into sublayers as shown in Fig. C1 with linear potential distribution across the thickness for each sublayer as presented in Wang (2004).

The electric potential field across the thickness can be defined as

$$\phi^k(z) = \mathbf{N}_\phi^k \bar{\boldsymbol{\phi}}^{\boldsymbol{k}} \tag{C.5}$$

where $\mathbf{N}_\phi^k$ is the shape function of the electric potential function and $\bar{\boldsymbol{\phi}}^{\boldsymbol{k}}$ denotes electric potential at top and bottom surfaces of the sublayer

$$\mathbf{N}_\phi^k = \frac{1}{t_i}[z - z_i\ z_{i+1} - z] \tag{C.6}$$

where t_i is the thickness of the sublayer. The electric field for each sublayer element is

$$\boldsymbol{E}^k = \boldsymbol{B}_\phi^k \bar{\boldsymbol{\phi}}^{\boldsymbol{k}} \tag{C.7}$$

where $\boldsymbol{B}_\phi^k = \frac{1}{t_i}[1\ \ -1]$ and $\bar{\boldsymbol{\phi}}^{\boldsymbol{k}} = [\boldsymbol{\phi}^{\boldsymbol{k}}\ \boldsymbol{\phi}^{\boldsymbol{k+1}}]^T$.

The element stiffness matrix as given in Junior et al. (2009) is

$$\boldsymbol{K} = \begin{pmatrix} \int_\Omega z^2 \boldsymbol{B_u}^T \bar{\boldsymbol{C}} \boldsymbol{B_u}\, g(\Psi(x))\, d\Omega & \int_\Omega z \boldsymbol{B_u}^T \bar{\boldsymbol{e}}^T \boldsymbol{B}_\phi\, g(\Psi(x))\, d\Omega \\ \int_\Omega z \boldsymbol{B}_\phi^T \bar{\boldsymbol{e}} \boldsymbol{B_u}\, g(\Psi(x))\, d\Omega & \int_\Omega \boldsymbol{B}_\phi^T \bar{\boldsymbol{\kappa}} \boldsymbol{B}_\phi\, g(\Psi(x))\, d\Omega \end{pmatrix} \tag{C.8}$$

$\bar{\boldsymbol{C}}$, $\bar{\boldsymbol{e}}$ and $\bar{\boldsymbol{\kappa}}$ are the plane stress (2D) constants in terms of 3D material constants (Junior et al., 2009). The "ersatz material" approach is adopted to model the voids. The stiffness matrix is obtained by numerically integrating over subtriangles on either sides of the inclusion interface. Replacing voids by a weak material, helps the optimization algorithm to recover from trial topologies in which the void boundary intersects with force boundary.

Note that enrichment functions are not used and so there is no change in the degrees of freedom with iterations in the optimization process. As suggested in Li et al. (2012) $g(\Psi(x))$ is taken as

$$g(\Psi(x)) = \begin{cases} 1 & \Psi(x) \geq 0 \\ 1e-4 & \Psi(x) < 0 \end{cases} \tag{C.9}$$

The piezoelectric nano plate (PNP) exhibits different surface elastic and surface piezoelectric behavior compared to the bulk. The PNP may be assumed to be a bulk plate with surface elastic constants and surface piezoelectric constants at the top and bottom sublayers of the discretization for electric potential field.

The surface stiffness matrix may be defined as

$$\boldsymbol{K_s} = \begin{pmatrix} \int_{\Omega_s} z^2 \boldsymbol{B_u}^T (\bar{\boldsymbol{C}} + \bar{\boldsymbol{C}}_{\boldsymbol{s}}) \boldsymbol{B_u}\, d\Omega_s & \int_{\Omega_s} z \boldsymbol{B_u}^T (\bar{\boldsymbol{e}}^T + \bar{\boldsymbol{e}}_{\boldsymbol{s}}^T) \boldsymbol{B}_\phi\, d\Omega_s \\ \int_{\Omega_s} z \boldsymbol{B}_\phi^T (\bar{\boldsymbol{e}} + \bar{\boldsymbol{e}}_{\boldsymbol{s}}) \boldsymbol{B_u}\, d\Omega_s & \int_{\Omega_s} \boldsymbol{B}_\phi^T (\bar{\boldsymbol{\kappa}} + \bar{\boldsymbol{\kappa}}_{\boldsymbol{s}}) \boldsymbol{B}_\phi\, d\Omega_s \end{pmatrix} \tag{C.10}$$

where $\boldsymbol{\Omega}_s$ corresponds to the top and bottom sublayers, z is the distance of the mid-surface of the top/bottom sublayers from the neutral surface. $\bar{\boldsymbol{C}}_{\boldsymbol{s}}$, $\bar{\boldsymbol{e}}_{\boldsymbol{s}}$ and $\bar{\boldsymbol{\kappa}}_{\boldsymbol{s}}$ are the surface elastic, piezoelectric and dielectric constants:

$$\begin{aligned}
\boldsymbol{K}_{\boldsymbol{uu}}^{\boldsymbol{b}} &= \int_{\Omega_s} z^2 \boldsymbol{B_u}^T (\bar{\boldsymbol{C}}) \boldsymbol{B_u}\, d\Omega_s \\
\boldsymbol{K}_{\boldsymbol{uu}}^{\boldsymbol{s}} &= \int_{\Omega_s} z^2 \boldsymbol{B_u}^T (\bar{\boldsymbol{C}}_{\boldsymbol{s}}) \boldsymbol{B_u}\, d\Omega_s \\
\boldsymbol{K}_{\boldsymbol{u\phi}}^{\boldsymbol{b}} &= \int_{\Omega_s} z \boldsymbol{B_u}^T (\bar{\boldsymbol{e}}^T) \boldsymbol{B}_\phi\, d\Omega_s = \boldsymbol{K}_{\boldsymbol{\phi u}}^{\boldsymbol{b}\ T} \\
\boldsymbol{K}_{\boldsymbol{u\phi}}^{\boldsymbol{s}} &= \int_{\Omega_s} z \boldsymbol{B_u}^T (\bar{\boldsymbol{e}}_{\boldsymbol{s}}^T) \boldsymbol{B}_\phi\, d\Omega_s = \boldsymbol{K}_{\boldsymbol{\phi u}}^{\boldsymbol{s}\ T} \\
\boldsymbol{K}_{\boldsymbol{\phi\phi}}^{\boldsymbol{b}} &= \int_{\Omega_s} \boldsymbol{B}_\phi^T (\bar{\boldsymbol{\kappa}}) \boldsymbol{B}_\phi\, d\Omega_s \\
\boldsymbol{K}_{\boldsymbol{\phi\phi}}^{\boldsymbol{s}} &= \int_{\Omega_s} \boldsymbol{B}_\phi^T (\bar{\boldsymbol{\kappa}}_{\boldsymbol{s}}) \boldsymbol{B}_\phi\, d\Omega_s
\end{aligned} \tag{C.11}$$

References

Agrawal, R., Espinosa, H.D., 2011. Giant piezoelectric size effects in zinc oxide and gallium nitride nanowires. A first principles investigation. Nano Lett. 11, 786–790.

Allaire, G., Jouve, F., Toader, A.M., 2004. Structural optimization using sensitivity analysis and a level-set method. J. Comput. Phys. 194, 363–393.

Chen, C.Q., Shi, Y., Zhang, Y.S., Zhu, J., Yan, Y.J., 2006. Size dependence of Young's modulus in zno nanowires. Phys. Rev. Lett. 96, 075505.

Chen, S., Gonella, S., Chen, W., Liu, W.K., 2010. A level set approach for optimal design of smart energy harvesters. Comput. Methods Appl. Mech. Eng. 199, 2532–2543.

Choi, K.K., Kim, N.H., 2005. Structural Sensitivity Analysis and Optimization. Springer, New York.

Dai, S., Park, H.S., 2013. Surface effects on the piezoelectricity of zno nanowires. J. Phys. Mech. Solids 61.

Dai, S., Gharbi, M., Sharma, P., Park, H.S., 2011. Surface piezoelectricity: size-effects in nanostructures and the emergence of piezoelectricity in non-piezoelectric materials. J. Appl. Phys. 110, 104305.

Espinosa, H.D., Bernal, R.A., Minary-Jolandan, M., 2012. A review of mechanical and electromechanical properties of piezoelectric nanowires. Adv. Mater. 24, 4656–4675.

Farsad, M., Vernerey, F.J., Park, H.S., 2010. An extended finite element/level set method to study surface effects on the mechanical behavior and properties of nanomaterials. Int. J. Numer. Methods Eng. 84, 1466–1489.

Gurtin, M.E., Murdoch, A.I., 1975. A continuum theory of elastic material surfaces. Arch. Ration. Mech. Anal. 57, 291–323.

Gurtin, M.E., Weissmller, J., Larché, F., 1998. A general theory of curved deformable interfaces in solids at equilibrium. Philos. Mag. 75, 1093–1109.

Hoang, M.-T., Yvonnet, J., Mitrushchenkov, A., Chambaud, G., 2013. First-principles based multiscale model of piezoelectric nanowires with surface effects. J. Appl. Phys. 113.

Junior, C.D.M., Erturk, A., Inman, D.J., 2009. An electromechanical finite element model for piezoelectric energy harvester plates. J. Sound Vib. 327, 9–25.

Li, L., Wang, M.Y., Wei, P., 2012. XFEM schemes for level set based structural optimization. Front. Mech. Eng. 7 (4), 335–356.

Mitrushchenkov, A., Linguerri, R., Chambaud, G., 2009. Piezoelectric properties of AlN, ZnO, and $Hg_xZn_{1-x}O$ nanowires by first-principles calculations. J. Phys. Chem. C 113.

Moes, N., Dolbow, J., Belytschko, T., 1999. A finite element method for crack growth without remeshing. Int. J. Numer. Methods Eng. 46, 133–150.

Moes, N., Cloirec, M., Cartraud, P., Remacle, J.F., 2003. A computational approach to handle complex microstructure geometries. Comput. Methods Appl. Mech. Eng. 192, 3163–3177.

Momeni, K., Odegard, G.M., Yassar, R.S., 2012a. Finite size effect on the piezoelectric properties of zno nanobelts: a molecular dynamics approach. Acta Mater. 60.

Momeni, K., Odegard, G.M., Yassar, R.S., 2012b. Finite size effect on the piezoelectric properties of zno nanobelts: a molecular dynamics approach. Acta Mater. 60, 5117–5124.

Nakasone, P., Silva, E., 2009. Design of piezoelectric energy harvesting devices and laminate structures by applying topology optimization, modeling, signal processing, and control for smart structures. Proc. SPIE 728601–728611.

Nanthakumar, S.S., Lahmer, T., Rabczuk, T., 2013. Detection of flaws in piezoelectric structures using extended FEM. Int. J. Numer. Methods Eng. 96, 373–389.

Nanthakumar, S.S., Lahmer, T., Rabczuk, T., 2014. Detection of multiple flaws in piezoelectric structures using XFEM and level sets. Comput. Methods Appl. Mech. Eng. 275, 98–112.

Nanthakumar, S.S., Lahmer, T., Zhuang, X., Zi, G., Rabczuk, T., 2016. Detection of material interfaces using a regularized level set method in piezoelectric structures. Inverse Probl. Sci. Eng 24 (1), 153–176, http://dx.doi.org/10.1080/17415977.2015.1017485.

Osher, S.J., Sethian, J.A., 1988. Fronts propagating with curvature dependent speed: algorithms based on the Hamilton–Jacobi formulation. J. Comput. Phys. 79, 12–49.

Priya, S., 2007. Advances in energy harvesting using low profile piezoelectric transducers. J. Electroceram. 19, 167–184.

Priya, D.I.S., 2009. Energy Harvesting Technologies. Springer, US, http://dx.doi.org/10.1007/978-0-387-76464-1.

Rupp, C.J., Evgrafov, A., Maute, k., Dunn, M.L., 2009. Design of piezoelectric energy harvesting systems: a topology optimization approach based on multilayer plates and shells. J. Intell. Mater. Syst. Struct. 16, 1923–1939.

Silva, E.C.N., Kikuchi, N., 2007. Design of piezoelectric transducers using topology optimization. J. Electroceram. 19, 167–184.

Sodano, H.A., Inman, D.J., Park, G., 2004. A review of power harvesting from vibration using piezoelectric materials. Shock Vib. Dig. 36, 197–205.

Sukumar, N., Chopp, D.L., Moes, N., Belytschko, T., 2001. Modeling holes and inclusions by level sets in the extended finite-element method. Comput. Methods Appl. Mech. Eng. 190, 6183–6200.

Trinidade, M.A., Benjeddou, A., 2009. Effective electromechanical coupling coefficients of piezoelectric adaptive structures: critical evaluation and optimization. Mech. Adv. Mater. Struct. 16, 210–223.

Wang, S.Y., 2004. A finite element model for the static and dynamic analysis of a piezoelectric bimorph. Int. J. Solids Struct. 41, 4075–4096.

Wang, S.Y., 2012. Surface effects on the electroelastic responses of a thin piezoelectric plate with nanoscale thickness. J. Phys. D: Appl. Phys. 45, 255401.

Wang, Z.L., Song, J., 2006. Piezoelectric nanogenerators based on zinc oxide nanowire arrays. Science 312, 242–246.

Wang, M.Y., Wang, S.Y., 2006. Radial basis functions and level set method for structural topology optimization. Int. J. Numer. Methods Eng. 65, 2060–2090.

Wang, S.Y., Lim, K.M., Khoo, B.C., Wang, M.Y., 2007. An extended level set method for shape and topology optimization. J. Comput. Phys. 221, 395–421.

Wein, F., Kaltenbacher, M., Stingl, M., 2013. Topology optimization of a cantilevered piezoelectric energy harvester using stress norm constraints. Struct. Multidiscip. Optim. 48, 173–185.

Wendland, H., 1995. Piecewise polynomial, positive definite and compactly supported radial functions of minimal degree. Adv. Comput. Math. 4.1, 389–396.

Xu, S., Qin, Y., Xu, C., Wei, Y., Yang, R., Wang, Z.L., 2010. Self-powered nanowire devices. Nat. Nanotechnol. 5, 366–373.

Yan, Z., Jiang, L., 2011a. Surface effects on the electromechanical coupling and bending behaviours of piezoelectric nanowires. J. Phys. D: Appl. Phys. 44, 075404.

Yan, Z., Jiang, L.Y., 2011b. The vibrational and buckling behaviors of piezoelectric nanobeams with surface effects. Nanotechnology 22, 245703.

Yvonnet, J., Quang, H.L., He, Q.C., 2008. An xfem/level set approach to modelling surface/interface effects and to computing the size-dependent effective properties of nanocomposites. Comput. Mech. 42, 119–131.

Zhao, M.H., Wang, Z.L., Mao, S.X., 2004. Piezoelectric characterization of individual zinc oxide nanobelt probed by piezoresponse force microscope. Nanoletters 4, 587–590.

Zheng, B., Chang, C., Gea, H., 2009. Topology optimization of energy harvesting devices using piezoelectric materials. Struct. Multidiscip. Optim. 38 (1), 17–23.